Selecting superluminous supernovae in faint galaxies from the first year of the Pan-STARRS1 Medium Deep Survey

Monthly Notices
of the
ROYAL ASTRONOMICAL SOCIETY

MNRAS **448,** 1206–1231 (2015) doi:10.1093/mnras/stv034

Selecting superluminous supernovae in faint galaxies from the first year of the Pan-STARRS1 Medium Deep Survey

M. McCrum,[1]★ S. J. Smartt,[1] A. Rest,[2] K. Smith,[1] R. Kotak,[1] S. A. Rodney,[3]† D. R. Young,[1] R. Chornock,[4] E. Berger,[4] R. J. Foley,[4] M. Fraser,[1] D. Wright,[1] D. Scolnic,[3] J. L. Tonry,[5] Y. Urata,[6] K. Huang,[7] A. Pastorello,[8] M. T. Botticella,[9] S. Valenti,[10,11] S. Mattila,[12] E. Kankare,[12] D. J. Farrow,[13] M. E. Huber,[5] C. W. Stubbs,[4] R. P. Kirshner,[4] F. Bresolin,[5] W. S. Burgett,[5] K. C. Chambers,[5] P. W. Draper,[13] H. Flewelling,[5] R. Jedicke,[5] N. Kaiser,[5] E. A. Magnier,[5] N. Metcalfe,[13] J. S. Morgan,[5] P. A. Price,[5] W. Sweeney,[5] R. J. Wainscoat[5] and C. Waters[5]

[1]*Astrophysics Research Centre, School of Maths and Physics, Queen's University Belfast, Belfast BT7 1NN, UK*
[2]*Space Telescope Science Institute, 3700 San Martin Drive, Baltimore, MD 21218, USA*
[3]*Department of Physics and Astronomy, Johns Hopkins University, 3400 North Charles Street, Baltimore, MD 21218, USA*
[4]*Department of Physics, Harvard University, Cambridge, MA 02138, USA*
[5]*Institute for Astronomy, University of Hawaii at Manoa, Honolulu, HI 96822, USA*
[6]*Institute of Astronomy, National Central University, Chung-Li 32054, Taiwan*
[7]*Department of Mathematics and Science, National Taiwan Normal University, Lin-kou District, New Taipei City 24449, Taiwan*
[8]*INAF–Osservatorio Astronomico di Padova, Vicolo dell'Osservatorio 5, I-35122 Padova, Italy*
[9]*INAF–Osservatorio astronomico di Capodimonte, Salita Moiariello 16, I-80131 Napoli, Italy*
[10]*Las Cumbres Observatory Global Telescope Network, 6740 Cortona Drive, Suite 102, Goleta, CA 93117, USA*
[11]*Department of Physics, University of California Santa Barbara, Santa Barbara, CA 93106, USA*
[12]*Finnish Centre for Astronomy with ESO (FINCA), University of Turku, Väisäläntie 20, FI-21500 Piikkiö, Finland*
[13]*Department of Physics, Durham University, South Road, Durham DH1 3LE, UK*

Accepted 2015 January 6. Received 2014 November 7; in original form 2014 February 3

ABSTRACT

The Pan-STARRS1 (PS1) survey has obtained imaging in five bands ($grizy_{P1}$) over 10 Medium Deep Survey (MDS) fields covering a total of 70 square degrees. This paper describes the search for apparently hostless supernovae (SNe) within the first year of PS1 MDS data with an aim of discovering superluminous supernovae (SLSNe). A total of 249 hostless transients were discovered down to a limiting magnitude of $M_{AB} \sim 23.5$, of which 76 were classified as Type Ia supernovae (SNe Ia). There were 57 SNe with complete light curves that are likely core-collapse SNe (CCSNe) or type Ic SLSNe and 12 of these have had spectra taken. Of these 12 hostless, non-Type Ia SNe, 7 were SLSNe of type Ic at redshifts between 0.5 and 1.4. This illustrates that the discovery rate of type Ic SLSNe can be maximized by concentrating on hostless transients and removing normal SNe Ia. We present data for two possible SLSNe; PS1-10pm ($z = 1.206$) and PS1-10ahf ($z = 1.1$), and estimate the rate of type Ic SLSNe to be between $3^{+3}_{-2} \times 10^{-5}$ and $8^{+2}_{-1} \times 10^{-5}$ that of the CCSN rate within $0.3 \leq z \leq 1.4$ by applying a Monte Carlo technique. The rate of slowly evolving, type Ic SLSNe (such as SN2007bi) is estimated as a factor of 10 lower than this range.

Key words: supernovae: general – supernovae: individual: PS1-10pm – supernovae: individual: PS1-10ahf.

1 INTRODUCTION

Optical transients which are spatially coincident or associated with elongated and extended sources have a high probability of being

★ E-mail: mmccrum04@qub.ac.uk
† Hubble Postdoctoral Fellow.

supernovae (SNe). Thus, when searching for SNe, concentrating on high mass or intrinsically high luminosity galaxies can be a fruitful endeavour to optimize the yield of recorded events as it will maximize the number of stars observed that can potentially explode as SNe. To date the majority of such searches at low redshift have adopted this approach to good effect, for example the Lick Observatory Supernova Search (Leaman et al. 2011). The unbiased nature of surveys like the Palomar Transient Factory (PTF; Arcavi et al. 2010) and Pan-STARRS1 (PS1; Kaiser et al. 2010) mean that transients are being discovered without a bright galaxy bias and the neighbourhoods in which SNe are being found are not restricted to large, star-forming galaxies. Arcavi et al. (2010) found that the core-collapse SNe (CCSNe) population in dwarf galaxies is different to that found in giant galaxies, in the sense that there are many more broad-lined, Type Ic supernovae (SNe Ic) in the former population. They link this to the metallicity of the underlying stellar population and its effect on stellar evolution.

Another class of SNe that have so far been discovered almost exclusively hosted by smaller, fainter galaxies is the relatively rare breed of superluminous supernovae (SLSNe). Quimby et al. (2011) unravelled the mysteries of the luminous SN2005ap and SCP 06F6 by grouping them with a number of PTF discoveries to suggest these SLSNe as the death throes of at least some of the most massive of stars. Detailed studies of some of these events, such as SN2010gx (also known as PTF10cwr; Pastorello et al. 2010a; Quimby et al. 2011) and PTF12dam (Nicholl et al. 2013), have increased the knowledge based on these highly energetic events and the recent PS1 discoveries of PS1-10ky, PS1-10awh (Chomiuk et al. 2011), PS1-10bzj (Lunnan et al. 2013) and PS1-11ap (McCrum et al. 2014) are supporting and expanding progenitor and physical explosion mechanism theories. The highest redshift discoveries ($z > 1.5$) from PS1 of Berger et al. (2012) and from the Supernova Legacy Survey (Howell et al. 2013) illustrate that SLSNe can be spectroscopically followed at significantly higher redshifts than SNe Ia.

Quimby et al. (2011) used the identification of narrow Mg II $\lambda\lambda$2796, 2803 absorption lines from foreground gas to place robust lower limits on the redshift of these SLSNe, which immediately provided an estimate of the enormous luminosities. In a few cases, the redshifts of the Mg II absorption exactly match the emission lines of the host galaxy, confirming the reasonable assumption that the Mg II absorption arises in the host galaxy itself. The redshifts derived by Quimby et al. (2011) and then by Chomiuk et al. (2011) using this method find peak absolute SLSNe magnitudes of $M_u \simeq -22 \pm 0.5$ mag and total radiated energies $\gtrsim 10^{51}$ erg, making them substantially more luminous than any other SN-type events.

Despite this common lower limit, differences in the photometric and spectroscopic evolution of the observed SLSNe suggests a number of progenitor possibilities. Pastorello et al. (2010a) find iron and other features normally associated with SNe Ic in the spectra of SN2010gx at 30–50 d after peak showing that the transient evolved to resemble an energetic SN Ic but on a much slower time-scale. Inserra et al. (2013) present data on another five such objects at redshifts 0.1–0.2 with detailed modelling suggesting that the explosions are simply 'normal' SNe Ic with an additional power source providing a boost to the luminosity. The best-fitting models presented by Inserra et al. (2013) are those where a fast rotating neutron star (magnetar) provides the extra energy required, an idea proposed and developed by Ostriker & Gunn (1971), Thompson, Chang & Quataert (2004) and Kasen & Bildsten (2010). Other power sources, such as the radioactive decay of ^{56}Ni (Arnett 1982), are also explored but could not be reconciled with the light curves of SLSNe. These kind of models were used by Nicholl et al. (2013) and McCrum et al. (2014) to explain the slower photometric evolution of the SLSNe PTF12dam and PS1-11ap, where again the magnetar models gave the most satisfactory fits to the data. Prior to the discovery of these two SLSNe however, the only well-studied object of this slowly evolving type was SN2007bi (Gal-Yam et al. 2009; Young et al. 2010) which was believed to have been the result of a pair-instability supernova (Fowler & Hoyle 1964; Barkat, Rakavy & Sack 1967; Bond, Arnett & Carr 1984; Heger & Woosley 2002). Chevalier & Irwin (2011) suggest the interaction of the SN shock with a dense circumstellar material of H-poor material as a possible mechanism for the production of the observed features of the light curves and spectra. This theory also accounts for the Ic-like features and the unusually high magnitudes associated with the aforementioned objects. Thus, we will refer to these two subclasses of SLSNe, those sharing the properties of the Quimby et al. (2011) sample and those that display the prolonged light-curve evolution of SN2007bi, as SLSNe Ic and slowly evolving SLSNe Ic, respectively.

A number of discoveries of a completely separate class of SLSNe that display strong H emission similar to the Type II classes of SNe have also been made. SN2006gy (Ofek 2007; Smith et al. 2007) and SN2003ma (Rest et al. 2011) are examples of this class, where the observed features are likely produced by the interaction between an energetic SN explosion and a very dense circumstellar medium. Any objects of this class will be referred to here as SLSNe II (Gal-Yam 2012). In contrast to the SLSNe Ic, SN2006gy and SN2003ma occurred in bright host galaxies, suggesting that SLSNe II do not follow the apparent trend visible for SLSNe Ic which have, almost exclusively, dwarf hosts.

An important feature of the known SLSNe Ic sample is the noticeable preference for them appearing in faint host galaxies. This trend has been apparent right from the early discoveries with a faint host galaxy of no brighter than $M_r \sim -18$ found for SN2005ap (Adami et al. 2006) and an upper limit of -18.1 mag set at the pre-explosion location of SCP06F6 (Barbary et al. 2009). Pastorello et al. (2010b) and Quimby et al. (2011) found a faint dwarf host for SN2010gx in archive Sloan Digital Sky Survey (SDSS) images (SDSS J112546.72−084942.0), with an absolute magnitude of $M_r \sim -18$ and a more recent study further refined this value to $M_g = -17.42 \pm 0.17$ (Chen et al. 2013). Young et al. (2010) also calculated an absolute magnitude for the host of SN2007bi using SDSS archive images (SDSS J131920.14+085543.7) and found an $M_B \sim -16.4$. A similar trend has been noted with virtually all subsequent discoveries (Barbary et al. 2009; Pastorello et al. 2010a; Chomiuk et al. 2011; Quimby et al. 2011; Leloudas et al. 2012; Chen et al. 2013; Lunnan et al. 2013; Nicholl et al. 2014), which led Lunnan et al. (2014) to study a large sample of host galaxies and suggest that they are similar hosts to those of gamma-ray bursts (GRBs). An exception to this supposed trend is the event so far reported with one of the highest redshifts. PS1-11bam (Berger et al. 2012), which has $z = 1.55$ derived from strong absorption of both Fe II and Mg II and the detection of [O II] 3727 Å from the host galaxy in emission, has the most luminous host discovered so far for an SLSN Ic, with a near-ultraviolet (NUV) absolute magnitude of $M_{\rm NUV} \simeq -20.3$. However, the host is still some two magnitudes fainter than the SN itself.

In summary, the currently known SLSNe Ic sample typically appear to be >2–4 mag brighter than their hosts (see Lunnan et al. 2014, for a compilation of host magnitudes) indicating that a simple way of isolating them in higher redshift searches could be to target transients with either no host detected or with a significant difference between total host luminosity and peak SLSN Ic magnitude. It is

striking that no SLSNe Ic erupting in bright galaxies have been uncovered by any previous wide-field survey or galaxy targeted low redshift searches. Although one might argue there is always a preference for observers to take spectra of isolated transients to avoid galaxy contamination effects, the very large sample of low redshift SNe now classified do not contain any examples of SLSNe Ic in galaxies close to L^* (the characteristic luminosity in the Schechter luminosity function for galaxies, approximately corresponding to $M_B \simeq -21$ Schechter 1976). This is somewhat surprising since the bulk of stellar mass, and star formation, occurs in galaxies close to L^*.

The focus of this paper is to use this apparent preference for dwarf galaxy hosts as a method of finding SLSNe Ic in the first year of the PS1 Medium Deep Survey (MDS), to quantify their numbers in a magnitude limited survey and to approximately estimate the volumetric rates between the redshift range of $z = 0.3$–1.4. Quimby et al. (2013a) previously estimated the SLSN Ic rate to be 32^{+77}_{-26} events Gpc^{-3} yr^{-1} h^3_{71} at a redshift of $z \sim 0.2$ (although based on 1 event) and the SLSN II rate to be 151^{+151}_{-82} events Gpc^{-3} yr^{-1} h^3_{71} at $z \sim 0.15$.

At the beginning of the PS1 survey, we used reference images which were made of a small number ($\sim$8) of single input images from a good night. As the survey has progressed we have been able to stack the images to build much deeper template and stack images. However, at the beginning of the PS1 survey and during the first year of operations, we used reference stacks which reached a limiting apparent magnitudes of $\sim$23.5 in the $g_{\rm P1} r_{\rm P1} i_{\rm P1}$ bands. Hence, SNe which are brighter than 22, but have no host visible brighter than 23.5 were immediately candidates for hunting down these exciting phenomena. This paper focuses on all hostless transients discovered during the first year of the PS1 survey operations.

2 THE PS1 MEDIUM DEEP SURVEY

The PS1 system is a high-étendue wide-field imaging system, designed for dedicated survey observations. The system is installed on the peak of Haleakala on the island of Maui in the Hawaiian island chain. The telescope has a 1.8-m diameter primary mirror and the gigapixel camera (GPC1) located at the $f/4.4$ cassegrain focus consists of sixty 4800 × 4800 pixel detectors (pixel scale 0.26 arcsec) giving a field of view of 3.3 diameter. Routine observations are conducted remotely, from the Waiakoa Laboratory in Pukalani. A more complete description of the PS1 system, both hardware and software, is provided by Kaiser et al. (2010). The survey philosophy and execution strategy are described in Chambers et al. (in preparation).

The PS1 observations are obtained through a set of five broadband filters, which we have designated as $g_{\rm P1}$, $r_{\rm P1}$, $i_{\rm P1}$, $z_{\rm P1}$, and $y_{\rm P1}$. Although the filter system for PS1 has much in common with that used in previous surveys, such as SDSS (Abazajian et al. 2009), there are important differences. The $g_{\rm P1}$ filter extends 20 nm redward of $g_{\rm SDSS}$, paying the price of 5577 Å sky emission for greater sensitivity and lower systematics for photometric redshifts, and the $z_{\rm P1}$ filter is cut off at 930 nm, giving it a different response than the detector response which defined $z_{\rm SDSS}$. SDSS has no corresponding $y_{\rm P1}$ filter. Further information on the passband shapes is described in Stubbs et al. (2010). The PS1 photometric system and its response is covered in detail in Tonry et al. (2012b). Photometry is in the 'natural' PS1 system, $m = -2.5\log(flux) + m'$, with a single zero-point adjustment m' made in each band to conform to the AB magnitude scale. This paper uses images and photometry from the PS1 MDS, the observations of which are described in more detail in Tonry et al. (2012a), Rest et al. (2014) and Scolnic et al. (2014). PS1 has observed 12 MDS fields, but we will only describe data from 10 of them (MD01 to MD10). MD00 is centred on M31 and we have not been searching systematically for SNe in this field behind Andromeda. MD11 was observed for a short period in 2010–2011, but has since been dropped from the MDS schedule. The MD field centres and the exposure times in the five filters are listed in Tables 1 and 2. Observations of between 3 and 5 MD fields are taken each night and the filters are cycled through in the following pattern : $g_{\rm P1}$ and $r_{\rm P1}$ in the same night (dark time), followed by $i_{\rm P1}$ and $z_{\rm P1}$ on the subsequent second and third night, respectively. Around full moon only $y_{\rm P1}$ data are taken. Any one epoch consists of eight dithered exposures of either 8 × 113 s for $g_{\rm P1}$ and $r_{\rm P1}$ or 8 × 240 s for the other three, giving nightly stacked images of 904 and 1920 s duration.

Table 1. PS1 Medium Deep field centres.

Field	RA (deg, J2000)	Dec. (deg, J2000)
MD00	10.675	41.267
MD01	35.875	−4.250
MD02	53.100	−27.800
MD03	130.592	44.317
MD04	150.000	2.200
MD05	161.917	58.083
MD06	185.000	47.117
MD07	213.704	53.083
MD08	242.787	54.950
MD09	334.188	0.283
MD10	352.312	−0.433
MD11	270.000	66.561

Table 2. PS1 MDS, typical cadence. FM ± 3 designates three nights on either side of full moon.

Night	Filter	Exposure time
1	$g_{\rm P1}$ & $r_{\rm P1}$	8 × 113s each
2	$i_{\rm P1}$	8 × 240 s
3	$z_{\rm P1}$	8 × 240 s
Repeats...	...	...
FM±3	$y_{\rm P1}$	8 × 240 s

Images obtained by the PS1 system are processed through the Image Processing Pipeline (IPP; Magnier 2006), on a computer cluster at the Maui High Performance Computer Center (MHPCC). The pipeline runs the images through a succession of stages including device 'de-trending', a flux-conserving warping to a sky-based image plane, masking and artefact location. De-trending involves bias and dark correction and flat-fielding using white light flat-field images from a dome screen, in combination with an illumination correction obtained by rastering sources across the field of view. After determining an initial astrometric solution the flat-fielded images were then warped on to the tangent plane of the sky using a flux conserving algorithm. The plate scale for the warped images was originally set at 0.200 arcsec pixel^{-1}, but has since been changed to 0.25 arcsec pixel^{-1} in what is known internally as the V3 tessellation for the MD fields. Bad pixel masks are applied to the individual images and carried through the stacking stage to give the 'nightly stacks' of 904 and 1920 s total duration.

2.1 Image subtraction pipelines

We have had two parallel difference image pipelines running since the start of full PS1 science operations in 2010 May. The PHOTPIPE pipeline (Rest et al. 2005) is hosted at Harvard/CfA and this is the primary source of the final photometry presented in this paper. We briefly outline the process below, but the reader is referred to Rest et al. (2014) for a full description of this pipeline. This pipeline produces difference images from the MD nightly stacks compared to a deep, good image quality reference made from pre-season data. Forced-centroid, point spread function (PSF)-fitting photometry is applied on its difference images, with a PSF derived from reference stars in each nightly stack. The zero-points were measured for the AB system from comparison with field stars in the SDSS catalogue. We propagate the Poisson error on the pixel values through the resampling and difference imaging. Since this does not take the covariance between neighbouring pixels into account, we also do forced photometry in apertures at random positions and calculate the standard deviation of the ratio between the flux and the error. We then multiply all errors by the standard deviation to correct for the covariance. Nightly difference images typically yield 3σ limiting magnitudes of $\sim$23.5 mag in $g_{\rm P1}$, $r_{\rm P1}$, $i_{\rm P1}$ and $z_{\rm P1}$.

In parallel, the PS1 system has developed the Transient Science Server (TSS) which uses the difference imaging and photometric data from the IPP running in Hawaii. This process was described initially in Gezari et al. (2012) and is repeated here, expanded upon for completeness. The TSS automatically takes the nightly stacks created by the IPP in the MHPCC, creates difference images with manually created reference images, carries out PSF fitting photometry on the difference images and returns catalogues of variables and transient candidates. In the current version, forced photometry is not implemented. Mask and variance arrays are carried forward at each stage of the IPP processing. Photometric and astrometric measurements performed by the IPP system are described in Magnier (2007) and Magnier et al. (2008), respectively. Individual detections made on the difference images are copied nightly from the MHPCC and ingested into a MySQL data base (located at Queen's University) after an initial culling of objects based on the detection of saturated, masked or suspected defective pixels within the PSF area. Sources detected on the nightly difference images are assimilated into potential real astrophysical transients based on a set of quality tests. The TSS requires more than three quality detections within the last seven observations of the field, including detections in more than one filter, and a root mean square (rms) scatter in the positions of ≤ 0.5 arcsec. Each of these quality detections must be of 5σ significance (defined as an instrumental magnitude error < 0.2 mag) *and* have a Gaussian morphology ($XY_{\rm moments} < 1.2$). Transient candidates which pass this automated filtering system are promoted for human screening, which currently runs at around 10 per cent efficiency (i.e. 10 per cent of the transients promoted automatically are judged to be real after human screening).

The overlap with the PHOTPIPE system is good, with most high significance, real transients found by both pipelines. Each pipeline has been used to inform the other of small numbers missed and the reasons. Within the PS1 TSS, real transients are cross-matched with all available catalogues of astronomical sources in the MDS fields (e.g. SDSS, GSC, 2MASS, APM, Veron AGN and X-ray catalogues) in order to have a first pass classification of SNe, variable star, active galactic nuclei (AGN) and nuclear transients. While the difference imaging runs within the PS1 IPP system in the MHPCC, the TSS data base is hosted at Queen's University Belfast. The long-term goal is to fully integrate the TSS into the PS1 system in Hawaii.

3 THE TRANSIENT SAMPLE

From the period starting 2010 February 25 and ending 2011 July 9, 249 hostless transients or 'orphans' were discovered in the PS1 Medium Deep fields. For the practical purposes of this paper, which will become clear for our scientific motivations, an orphan is defined as an object that is $>$3.4 arcsec away from the centre of a catalogued galaxy or point source brighter than approximately 23.5 mag (in any of the $g_{\rm P1}r_{\rm P1}i_{\rm P1}$ filters that the transient was detected in). This magnitude limit was chosen for two reasons. At the beginning of the search period in 2010 the limit of a reference stack was not significantly deeper than the nightly stack, hence the transients which were observed as hostless by definition had no host brighter than 23.5 mag in the specific band that they were detected in. Although the reference stacks now reach around 1 mag deeper, this limit is still useful as the transients we discuss in this paper are typically brighter than 22–22.5 mag, hence significantly brighter than the their hosts. In many cases, deeper images (Lunnan et al. 2014) or deep PS1 stacks (Tonry et al. 2012a) do indeed reveal a host or stellar counterpart. Deep imaging in the z band with the *Subaru* telescope revealed hosts for five of our orphans with magnitudes listed in the Appendix in Table A1. As can be seen in the table, two of these transients do have hosts brighter than 23.5 mag in the z band. Whilst our definition of 'hostless' here is somewhat arbitrary, it is reasonably well defined and serves the science motivations of this paper well as we shall see.

We set out with a goal of spectroscopically classifying as many of this hostless sample as possible, which peaked brighter than approximately 22–22.5 in any of the $g_{\rm P1}r_{\rm P1}i_{\rm P1}$ filters. This magnitude limit was chosen as a practical limit of the largest aperture telescopes (8 m) that we had significant access to. The primary source was the Gemini observatory, for which we had UK, USA and UH time access although we also used the UK resources of the 4.2 m William Herschel Telescope (WHT) and the CfA Harvard access to Magellan and the Multimirror Telescope. A combination of the finite time resources available for these spectroscopic programme, ambient weather conditions, field visibility and scheduling, meant that spectra could not be obtained for every transient brighter than our chosen limit. The general PS1 spectroscopic follow-up of transients is also described in Rest et al. (2014) and we emphasize that during the period described here, there were several multipurpose spectroscopic classification and follow-up programmes running at these facilities which combined extensive classification with follow-up of scientifically interesting targets. Due to the ease of observing hostless transients (because of a lack of host galaxy contamination), a significant effort was invested to classify as many as possible. The results of the spectroscopic classification programmes are listed in Tables 3 and 5 (virtually all of the Type Ia sample are discussed in the cosmological analysis of Rest et al. 2014).

This sample is of course not spectroscopically complete, as illustrated in Fig. 1. Our next step was to attempt photometric classification of those SNe for those which we did not manage to get spectra, but for which we had well-sampled and relatively complete light curves. This sample included all those candidates for which we were not able to take spectra and also those which had peak magnitudes too faint for inclusion in the spectroscopic typing programmes. We did not use this photometric fitting method for selecting targets for spectroscopy, since the light-curve fitting methods (PSNID and SOFT) require a well-sampled and complete light curve which obviously is not available when a spectrum needs to be triggered around peak brightness. As expected, the distribution for the photometrically classified objects peaks at about a magnitude fainter than that of the

Table 3. 28 spectroscopically confirmed PS1 SN Ia. For the objects marked with an '*', the spectral classifications for these as SNe Ia can be found in Rest et al. (2014). The MD06 object PS1-11acn is designated as PTF11dws in the cited source of classification.

Field	PS1 ID	RA (deg, J2000)	Dec. (deg, J2000)	z_{SPEC}	Peak r_{P1}	Telescope	Date	Ref.
MD01	PS1-10nu	36.8001	−4.5347	0.065	18.276 (0.004)	Magellan	14/08/2010	*
MD01	PS1-11cn	35.7730	−3.6101	0.250	20.866 (0.028)	GN	31/01/2011	*
MD03	PS1-1000026	129.0524	44.0071	0.140	20.370 (0.025)	WHT	23/02/2010	Valenti et al. (2010)
MD03	PS1-10bka	131.6802	44.0035	0.247	22.179 (0.096)	GN	31/01/2011	*
MD03	PS1-10bzt	132.2495	44.8656	0.420	22.291 (0.224)	MMT	28/12/2010	*
MD04	PS1-10iv	150.5018	2.0604	0.369	21.478 (0.055)	GN	14/05/2010	*
MD04	PS1-10l	151.2314	2.5908	0.370	23.435 (0.201)	Magellan	20/01/2010	*
MD04	PS1-11s	150.7889	2.143	0.400	22.251 (0.091)	Magellan	12/01/2011	*
MD04	PS1-11t	150.5261	2.0877	0.450	21.863 (0.093)	Magellan	12/01/2011	*
MD04	PS1-11p	148.7919	1.7302	0.480	22.372 (0.132)	Magellan	12/01/2011	*
MD04	PS1-11bh	149.6284	2.8717	0.350	21.830 (0.072)	Magellan	12/01/2011	*
MD05	PS1-10ix	162.0978	57.1481	0.381	21.950 (0.283)	GN	14/05/2010	*
MD06	PS1-11acn	184.7782	47.3557	0.150	20.079 (0.010)	Keck	13/06/2011	Gal-Yam et al. (2011)
MD06	PS1-10kj	183.5271	46.9923	0.350	22.136 (0.106)	MMT	18/06/2010	*
MD06	PS1-11jo	184.0016	47.9204	0.330	21.632 (0.045)	MMT	23/02/2011	*
MD06	PS1-11xw	184.9750	48.1402	0.270	21.318 (0.042)	MMT	11/06/2011	*
MD06	PS1-11yr	186.5881	46.5959	0.530	22.573 (0.131)	GN	11/06/2011	*
MD07	PS1-10ig	211.8623	53.3429	0.260	20.891 (0.035)	MMT	04/04/2010	*
MD07	PS1-10iy	214.1196	54.0535	0.443	22.171 (0.124)	GN	15/05/2010	*
MD07	PS1-10iw	214.4605	52.8010	0.447	21.845 (0.092)	GN	15/05/2010	*
MD07	PS1-10kf	212.9905	52.0718	0.450	22.188 (0.133)	MMT	18/06/2010	*
MD07	PS1-10kv	212.6639	53.9895	0.530	22.242 (0.148)	GN	07/07/2010	*
MD07	PS1-11zd	214.6670	54.1830	0.100	19.214 (0.006)	WHT	08/06/2011	*
MD08	PS1-10jz	241.7032	54.9809	0.550	22.283 (0.145)	MMT	18/06/2010	*
MD08	PS1-10jv	244.4487	55.3022	0.360	21.586 (0.057)	MMT	17/06/2010	*
MD10	PS1-10bjz	353.2949	−1.2353	0.310	21.503 (0.175)	MMT	10/12/2010	*
MD10	PS1-10byj	353.3821	0.1340	0.511	22.136 (0.118)	GN	17/12/2010	*
MD10	PS1-10axm	353.3285	−0.9505	0.510	22.274 (0.224)	GN	16/10/2010	*

spectroscopic sample. The light-curve fitting is described below in Sections 3.1 and 3.2

At a canonical redshift of $z \sim 0.2$, the 3.4 arcsec separation corresponds to a minimum separation of ∼11 kpc. Sullivan et al. (2006) used a host-association algorithm to ensure that the SNe Ia under study were being associated with appropriate host galaxies. This was important for conclusions within the paper involving specific host galaxy properties, such as the star formation rate; however, for the purposes of this study the 3.4 arcsec separation parameter we defined was sufficient. Our motivation is simply that a transient has no apparent host, we are not concerned with finding the most likely offset galaxy. The two possibilities for these orphans are either that the host is fainter than $r_{P1} \sim 23.5$ or that the transient has been expelled by a nearby galaxy and has a long enough lifetime that it can travel >10 kpc before some energetic event generates sufficient luminosity to be captured by PS1. Due to the shorter life cycle of CCSNe, runaway transients are likely SNe Ia or at least some type of thermonuclear event involving a White Dwarf (WD; e.g. see the transients described in Perets et al. 2010, which are significantly offset from their likely host galaxies). The alternative, where the host galaxy is simply too faint to be imaged by PS1 suggests that the transient could be intrinsically bright or the galaxy intrinsically faint. For example, the host galaxy could be undetected simply because it is at a high redshift which places it beyond the PS1 detection limit. If the host were a typical $L^\star$ galaxy (but undetected due to distance) this would imply the transient has an AB magnitude $\lesssim -22$. Alternatively, the transient could have a typical core-collapse magnitude of $M_{AB} \sim -18$ and if the host galaxy is undetected then it is likely an intrinsically faint dwarf, possibly of low metallicity, but either way this combination has previously been found to be associated with SLSNe Ic (Chomiuk et al. 2011; Quimby et al. 2011). They are not always dwarf galaxies as indicated by the high-z discovery of Berger et al. (2012) but they are typically, with very few exceptions in the current SLSNe Ic sample, at least 2 mag brighter than their hosts. The small subset of events which do not meet this criterion are all at higher redshifts, possibly indicating trends of metallicity and luminosity in these younger galaxies. This is explored in greater detail in Section 5. As we show below, this search method allows a fairly straightforward way of identifying high-z, superluminous transients.

Through the spectroscopic classification programmes discussed above, optical spectra were taken for 40 orphans in total. While we would have liked to be spectroscopically complete to a defined magnitude limit (around 22 mag), spectroscopic facility access and weather constraints did not allow it. As with all spectroscopic programmes, there is some human preference that plays a role in target selection. In PS1, we have been particularly looking for transients that might be a high-z which could mean red colours and/or slow rise times. Later in the paper, we discuss an estimate of the volumetric rates of SLSNe and the spectroscopic completeness plays a role in this. The number of SLSNe in the transient set without spectra (Tables 6 and A2) is then the important question which we discuss in Section 5.2.

3.1 Hostless Type Ia supernovae

Of these 40 transients which were spectroscopically confirmed, 28 turned out to be SNe Ia at redshifts between approximately 0.2 and 0.7 and these are listed in Table 3. All but two of these are already presented in Rest et al. (2014), with one extra from Valenti et al.

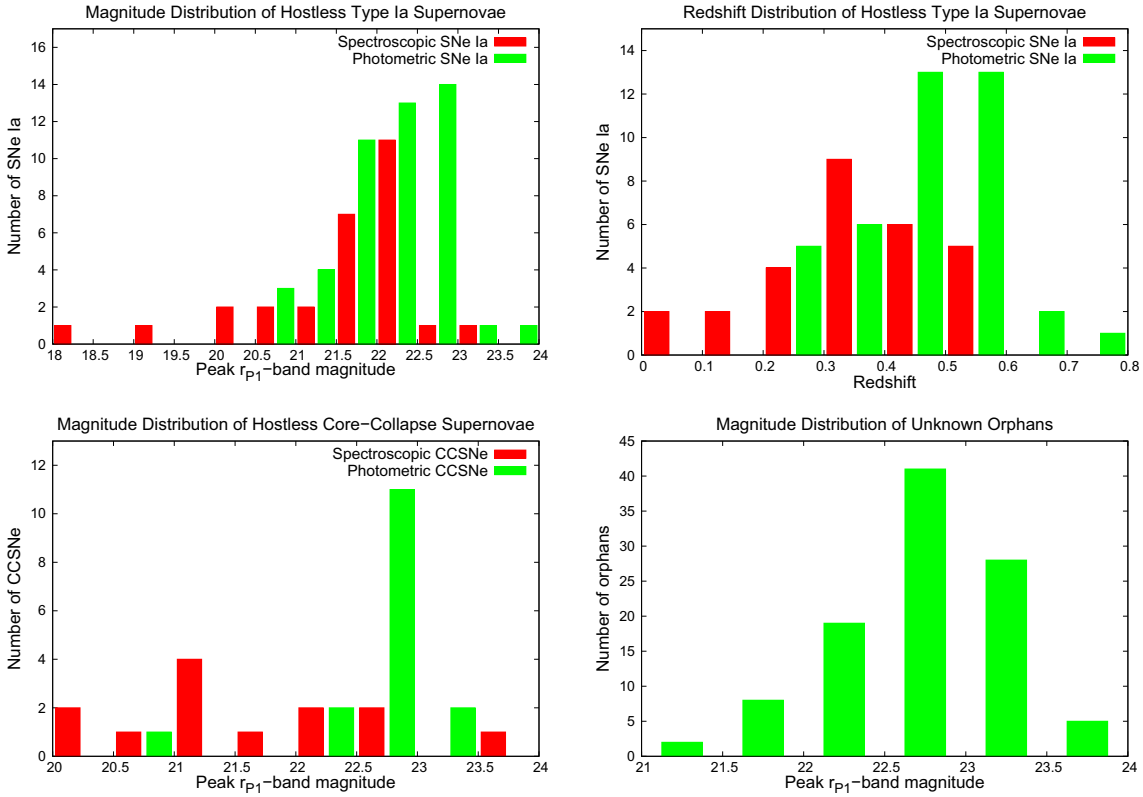

Figure 1. Magnitude (r_{P1} band) and redshift distributions of the SNe Ia orphans and magnitude distributions of the core-collapse orphans and the miscellaneous orphans. The classifications are split into two mutually exclusive classes, spectroscopic (red) classifications from a variety of telescopes and photometric (green) classifications using the SOFT and PSNID algorithms from Rodney & Tonry (2009) and Sako et al. (2008, 2011). Note that in the bottom-left panel there are 16 Photometric CCSNe, whereas Table 6 has 17. This is due to PS1-11ag not having r_{P1}-band points at peak, hence we do not plot it.

(2010) and one more which is the same object as discovered and reported by PTF (Gal-Yam et al. 2011).[1]

All transients for which no spectra were available (and which had relatively complete light curves) were passed through the SOFT and PSNID photoclassification algorithms (Sako et al. 2008, 2011; Rodney & Tonry 2009). We identified 48 SNe as having light curves matching SNe Ia between redshifts 0.2 and 0.7. In order to make these confident Type Ia classifications we initially demanded that *both* the SOFT and PSNID algorithms gave an SN Ia classification with a probability of > 80 per cent. This resulted in 40 SNe Ia, however we found a further eight that failed to get a secure classification in SOFT but PSNID returned a high probability of being an SN Ia. A visual inspection of these light curves suggests to us that they are plausible SNe Ia and all 48 photometrically classified SNe Ia are listed in Table 4.

The redshift values and their associated errors that are listed in this table are output from the SOFT photoclassification code. The method for generating these numbers is described in Rodney & Tonry (2010), including a figure comparing the photo-z of a test sample of SNe Ia against z values obtained from spectroscopic data. As can be seen in the paper, the rms scatter about $z_{\rm SOFT} = z_{\rm SPEC}$ is very small ($\sim$0.05) indicating that the photo-z values offer a fair approximation of the actual redshift values of the probable SNe in question.

[1] We thank Gal-Yam and Nugent for access to the spectrum to confirm classification.

In summary, through spectroscopy and light-curve fitting, we find that 76 of the orphan transient sample are confidently identified as SNe Ia.

3.2 Core-collapse and superluminous supernovae

The other 12 transients for which we gathered spectra are listed in Table 5 with their redshifts and classifications. Of these 12 spectroscopically confirmed SNe, there are four normal CCSNe, of types II, IIn and Ic. Chornock et al. (2013) presented the discovery of PS1-10afx at a redshift of $z = 1.388$, suggesting it to be an SLSN which is different to the currently known population. But this has now been shown to be more likely a normal SN Ia lensed by a foreground galaxy (Quimby et al. 2013b, 2014). We include it in Table 5 for completeness, as we originally had identified is a transient which was not obviously a normal SN Ia, although we do not use it any further in SLSN rate calculations. This leaves seven which are confirmed as SLSNe Ic, lying at redshifts beyond $z \sim 0.5$. These events include PS1-10pm and PS1-10ahf, the nature of which are discussed further in this paper. Detailed analysis of PS1-10ky, PS1-10awh, PS1-11ap can be found in Chomiuk et al. (2011) and McCrum et al. (2014). The classifications of PS1-11tt and PS1-11afv are presented in Lunnan et al. (2014) (and more details will be given in Lunnan et al., in preparation.). This immediately suggests quite a high fraction of SLSNe, if one could remove the SNe Ia from the sample efficiently and early enough.

There are another 45 transients for which we were unable to get spectroscopic confirmation, but have well-sampled and complete light curves which resemble CCSNe rather than SNe Ia. We passed

Table 4. 48 plausible PS1 SN Ia, classified using the SOFT and PSNID photometric classification codes (Sako et al. 2008, 2011; Rodney & Tonry 2009). The values in the SOFT and PSNID columns represent the probability that the object is classified as an SN Ia.

Field	PS1 ID	RA (deg, J2000)	Dec. (deg, J2000)	SOFT	PSNID	z_{PHOT}	dz	Peak r_{P1}
MD01	PS1-10aat	34.6005	−4.2033	–	0.999	–	–	22.532 (0.172)
MD01	PS1-10bcd	36.4632	−5.4049	0.996	0.974	0.480	0.028	22.289 (0.078)
MD01	PS1-10blx	35.2726	−3.8241	0.970	0.987	0.280	0.028	22.678 (0.181)
MD01	PS1-10zv	36.5108	−4.1125	–	1.000	–	–	21.421 (0.041)
MD01	PS1-10zz	36.8222	−3.2903	0.981	0.946	0.340	0.045	22.594 (0.104)
MD02	PS1-10afj	52.6562	−28.3717	–	0.987	0.260	0.028	22.948 (0.192)
MD02	PS1-10bxr	54.1715	−28.3673	0.890	0.998	0.460	0.117	22.483 (0.227)
MD03	PS1-10ayn	131.2068	43.8823	0.999	0.997	0.520	0.057	22.738 (0.132)
MD03	PS1-10bkm	129.6447	44.8684	–	1.000	–	–	21.510 (0.051)
MD03	PS1-10cbs	131.8921	44.5374	0.997	1.000	0.480	0.028	22.292 (0.116)
MD03	PS1-11bw	129.8787	43.9868	0.998	0.996	0.560	0.117	22.648 (0.178)
MD03	PS1-11ex	130.1915	43.8002	0.941	0.977	0.580	0.117	23.223 (0.165)
MD03	PS1-11gs	131.3379	44.6013	1.000	0.923	0.760	0.028	–
MD04	PS1-11du	149.6446	1.2582	0.876	0.819	0.620	0.117	23.599 (0.295)
MD04	PS1-11r	150.2982	1.5754	0.954	1.000	0.400	0.045	22.357 (0.105)
MD05	PS1-10uu	162.7694	58.4253	0.963	0.865	0.400	0.126	22.093 (0.122)
MD05	PS1-10wb	159.8594	57.2051	0.998	1.000	0.480	0.146	21.748 (0.296)
MD05	PS1-10jx	160.7420	56.9001	–	0.955	–	–	21.568 (0.055)
MD05	PS1-11bp	161.9585	57.2893	0.998	0.998	0.480	0.128	21.911 (0.112)
MD05	PS1-11oh	162.7667	59.1037	–	0.981	–	–	21.465 (0.067)
MD06	PS1-11ql	183.4322	46.2902	–	0.97	–	–	21.357 (0.054)
MD06	PS1-11tc	186.4050	46.7988	–	0.844	–	–	22.802 (0.316)
MD06	PS1-10qu	186.4676	47.8554	0.999	1.000	0.380	0.028	22.129 (0.103)
MD06	PS1-10qv	184.0243	47.3677	1.000	1.000	0.280	0.028	20.977 (0.049)
MD06	PS1-10rj	184.9626	47.7476	1.000	1.000	0.300	0.028	21.624 (0.065)
MD06	PS1-10tb	185.7344	46.9296	0.877	0.986	0.480	0.172	22.434 (0.134)
MD06	PS1-10wn	186.7645	46.8898	0.949	0.905	0.460	0.057	22.582 (0.219)
MD06	PS1-10xc	185.3965	46.0963	0.992	0.914	0.520	0.117	22.671 (0.120)
MD06	PS1-10xe	186.4073	46.7506	1.000	1.000	0.500	0.057	22.678 (0.127)
MD07	PS1-11nb	214.9577	53.3471	–	1.000	–	–	20.721 (0.030)
MD07	PS1-10lb	212.4660	53.7906	0.866	0.998	0.480	0.122	21.827 (0.081)
MD08	PS1-10acd	243.1638	55.0691	1.000	1.000	0.500	0.108	22.410 (0.181)
MD08	PS1-10aex	244.6181	55.2436	0.942	0.997	0.420	0.082	22.157 (0.131)
MD08	PS1-10afb	243.1847	56.0324	1.000	0.999	0.500	0.045	21.903 (0.077)
MD08	PS1-10afq	242.3236	56.4400	1.000	1.000	0.200	0.045	21.137 (0.054)
MD08	PS1-10lh	243.0192	56.1721	1.000	0.998	0.500	0.082	22.441 (0.168)
MD08	PS1-10nf	243.4779	54.1900	0.989	1.000	0.380	0.028	22.064 (0.149)
MD08	PS1-10np	240.4345	55.0052	1.000	0.954	0.540	0.100	22.521 (0.195)
MD08	PS1-10zo	240.3358	55.1399	0.988	0.997	0.520	0.146	21.927 (0.091)
MD09	PS1-10aac	334.6540	0.6184	1.000	1.000	0.600	0.028	21.970 (0.106)
MD09	PS1-10afi	333.5490	0.7323	0.964	0.957	0.500	0.072	22.868 (0.170)
MD09	PS1-10axb	332.6959	0.1951	0.947	0.966	0.520	0.141	22.663 (0.218)
MD09	PS1-10ayl	333.8780	−0.8293	0.983	0.985	0.460	0.072	22.956 (0.210)
MD09	PS1-10ls	333.9379	0.4928	0.999	0.990	0.420	0.057	22.408 (0.236)
MD09	PS1-10lw	333.2522	0.8601	0.979	0.959	0.500	0.028	21.869 (0.058)
MD09	PS1-10mi	334.6715	0.4075	1.000	0.997	0.360	0.161	22.440 (0.211)
MD10	PS1-10act	353.0132	0.6024	1.000	1.000	0.240	0.028	20.857 (0.033)
MD10	PS1-10lp	351.3700	−0.1235	1.000	1.000	0.360	0.045	21.646 (0.059)

these light curves through the PSNID and SOFT photoclassification algorithms, finding that 17 were classified as Type II by both algorithms with greater than 80 per cent confidence. These are listed in Table 6, and we propose that they are likely to be core-collapse, SNe II given the high confidence light-curve fits by both light-curve fitters. The other 28 transients had light curves which appeared SN-like but the fitting algorithms gave lower confidence levels for specific fits of SNe Ia, II or Ibc. These 28 transients are listed in Table A2, along with the lower confidence results from PSNID and SOFT. Additionally, a selection of these light curves are shown in Fig. A1 and show typical trends such as a single asymmetric peak or an extended, declining plateau. We propose that these are high confidence SNe but the classification of the light curve as SNe Ia, Ibc or II is uncertain.

Fig. 1 shows the magnitude distribution of the confirmed and plausible CCSNe, which again illustrates the spectroscopic and photometric limits of our sample. A simple conclusion from this is that if one selects orphan candidates from a wide-field, magnitude limited survey (such as the PS1 MDS) and one photometrically selects objects from the data stream with light curves which are unlike SNe Ia, then a large fraction of the brighter objects that remain are actually high redshift SLSNe Ic. Of course, there is still

Table 5. 12 confirmed PS1 CCSNe. Of note is the high percentage of SLSNe Ic confirmed. The two objects marked with an '*' are explored further in this paper. The RA and Dec. values are in the deg, J2000 format. The values in the SOFT and PSNID columns represent the probability that the object is classified as the SNe type given in brackets. The numbered references refer to the following papers: [1] McCrum et al. (2014), [2] this paper, [3] Lunnan et al. (2014), [4] Chomiuk et al. (2011), [5] Chornock et al. (2013), [6] Quimby et al. (2013a,b), [7] Quimby et al. (2014). PS1-10afx has been shown to be a lensed SN Ia, and is included here for completeness of objects, although we do not use it in any of our rate estimates.

Field	PS1 ID	RA	Dec.	Type	z_{SPEC}	SOFT	PSNID	Peak r_{P1}	Telescope	Date	Reference
MD05	PS1-11ap	162.1155	57.1526	SLSN Ic	0.524	–	1 (II)	20.217 (0.017)	NOT	07/02/2011	[1]
MD05	PS1-11ad	164.0876	57.6654	IIn	0.422	1 (II)	0.992 (II)	20.935 (0.053)	GN	15/02/2011	[2]
MD06	PS1-10pm*	183.1758	46.9915	SLSN Ic	1.206	1 (II)	1 (II)	22.090 (0.141)	GN	03/06/2010	[2]
MD06	PS1-11afv	183.9074	48.1801	SLSN Ic	1.407	–	–	22.211 (0.186)	GN	09/07/2011	[3]
MD07	PS1-11yh	212.7977	51.9868	II	0.146	–	–	21.189 (0.048)	MMT	05/06/2011	[2]
MD08	PS1-11tt	243.1907	54.0713	SLSN Ic	1.283	–	–	22.654 (0.167)	GN	07/06/2011	[3]
MD09	PS1-10ky	333.4076	1.2398	SLSN Ic	0.956	–	–	21.190 (0.077)	GN	17/07/2010	[4]
MD09	PS1-10afx	332.8507	0.1621	Lensed SN Ia	1.388	0.999 (Ibc)	–	23.730 (0.200)	GS	06/09/2010	[5,6,7]
MD09	PS1-10ahq	333.5172	1.1084	Ic	0.283	1 (Ibc)	1 (Ibc)	21.474 (0.046)	MMT	18/10/2010	[2]
MD09	PS1-10awh	333.6242	−0.0676	SLSN Ic	0.908	1 (II)	–	21.607 (0.075)	GN	12/10/2010	[4]
MD10	PS1-10acl	352.4529	−0.2916	IIn	0.260	–	–	21.313 (0.054)	MMT	08/10/2010	[2]
MD10	PS1-10ahf*	353.1180	−0.3621	SLSN Ic	1.1	1 (II)	1 (II)	22.680 (0.158)	GS	11/06/2010	[2]

Table 6. 17 plausible PS1 CCSNe. The values in the SOFT and PSNID columns represent the probability that the object is classified as the type II subclass listed.

Field	PS1 ID	RA (deg, J2000)	Dec. (deg, J2000)	Type	SOFT	PSNID	Peak r_{P1}
MD01	PS1-10acp	35.4861	−3.8369	IIL	1	1	22.699 (0.147)
MD01	PS1-10add	35.0764	−4.1370	IIP	1	1	22.170 (0.080)
MD03	PS1-10axq	130.5385	44.5480	IIL	1	1	22.929 (0.154)
MD04	PS1-10dq	150.2418	2.2475	IIP	1	1	22.568 (0.128)
MD04	PS1-11ag	149.2396	3.2529	IIL	1	1	–
MD04	PS1-11er	149.1978	2.4177	IIL	0.959	0.999	23.427 (0.340)
MD06	PS1-10sq	186.3077	46.6273	IIL	1	0.996	22.624 (0.133)
MD06	PS1-10vu	184.9374	46.1197	IIL	0.999	0.804	22.642 (0.107)
MD07	PS1-10wk	211.6645	52.4217	IIP	1	1	22.515 (0.140)
MD08	PS1-10acq	244.6603	55.1885	IIP	1	0.999	22.880 (0.331)
MD09	PS1-10aal	334.1762	−0.5736	IIL	1	1	22.358 (0.139)
MD09	PS1-10abf	334.0138	1.0291	IIL	1	1	23.431 (0.250)
MD09	PS1-10agf	334.7398	−0.1656	IIP	0.999	0.911	22.573 (0.328)
MD09	PS1-10aht	334.9031	1.2136	IIP	0.889	0.928	22.935 (0.201)
MD10	PS1-10acn	351.7261	−0.2600	IIL	1	1	22.985 (0.271)
MD10	PS1-10kz	351.2487	−0.3529	II	–	1	20.970 (0.032)
MD10	PS1-10ayg	350.9872	−0.3808	IIL	1	0.837	22.649 (0.118)

an outstanding question about how to identify the SNe Ia early enough in their light curve that one can securely identify them from photometry alone. This issue still remains open, but we show here that if it can be done then a large fraction of the transients brighter than about 22 mag are SLSNe Ic candidates.

One major caveat to this is that there may be more SLSN Ic candidates in the photometrically classified samples (either the Type Ia or core-collapse samples, or both), since the light-curve fitters do not contain SLSNe Ic (or SLSNe II) template light curves. As a check, we report the values output from SOFT and PSNID for the light curves of the spectroscopically confirmed, hostless CCSNe sample (see Table 5). None of the CCSNe sample were photometrically misclassified as SNe Ia, which supports our proposal that the sample in Table 4 is relatively pure.

However two of the SLSNe Ic would be misclassified as SNe II. Hence, it is possible that there are further SLSNe Ic masquerading as normal CCSNe in the objects in Tables 6 and A2. The lower-left-hand histogram in Fig. 1 again highlights the magnitude limit of approximately 22–22.5 in the spectroscopic observations. The spectroscopically confirmed sample peaks at a significantly brighter r_{P1}-band magnitude than the photometrically classified sample. It is therefore possible that some of the photometrically classified CCSNe presented in Table 6 could be unclassified SLSNe Ic. When we discuss the rates of SLSNe Ic, we note that they may be lower limits.

In summary, our spectroscopic follow-up programmes took spectra of 12 transients which were not SNe Ia. A large fraction of these (7) were confirmed to be SLSNe Ic at redshifts greater than $z \sim 0.5$, and another is an unusually luminous transient at $z = 1.388$. We photometrically classified 17 transients as plausible CCSNe and a further 28 had lower confidence photometric classifications.

3.3 Miscellaneous orphans

The remaining 116 hostless transients discovered by the PS1 survey have insufficient data for any reliable classification to be made due to light-curve data either being incomplete, variable or the object being too faint and only sneaking into the limiting magnitude the

survey can reach. As can be seen in the lower-right-hand plot in Fig. 1 these objects represent the fainter end of the detected orphans and so only limited data are currently available concerning them. A typical trend seen in some of these orphans is that of a discrete peak suggesting that some of the objects are at a high redshift and peak just above our magnitude limit giving us an incomplete light curve. It is probable that these are SNe or SNe-like transients. It is interesting to note that the spectroscopically and photometrically classified samples do not contain any obvious AGN or QSO type variable sources, suggesting that the likelihood of finding such black hole driven events is low if an underlying galaxy is not detected. We find many AGN and QSO variables in the full PS1 MDS transient search, but imposing the requirement for a host brighter than ∼23.5 does seem to reduce their detected frequency.

4 SLSNE IC ANALYSIS

4.1 PS1-10pm

PS1-10pm was first detected with PS1 in the $r_{\rm P1}$ band on MJD 55248 (2010 February 24) in MD06 at a location of RA = $12^{\rm h}12^{\rm m}42\overset{\rm s}{.}18$, Dec. = $46^\circ59'29\overset{''}{.}5$ (J2000). Detections in $griz_{\rm P1}$ continued until a final $z_{\rm P1}$-band point on MJD 55367 (2010 June 20) when the MD06 season ended and PS1 no longer continued to observe the object. Further data were taken on the 2010 July 7 with the ACAM instrument at the WHT (*griz*) and deep imaging in *i* and *z* was performed with the GMOS instrument on Gemini North (GN) on the 2011 January 30. The details of the photometry performed can be found in Table 7. The transient was caught as it began to rise and the PS1 coverage captures a reasonably well-defined peak. Fig. 2 shows observed $griz_{\rm P1}$ light curves for PS1-10pm.

Spectra of PS1-10pm were obtained with GMOS on GN on the 2010 June 3 and the July 2.[2] The first spectrum was taken using the R400 grating with a *GG*455 filter and a single, 2400 s exposure gave a signal-to-noise ratio (SNR) in the detected continuum of ∼10 per pixel (at approximately 6500 Å). With the R400 grating, a 1 arcsec slit provides a resolution of 7.9 Å and the actual useful wavelength range of the obtained spectrum was from ∼5000 to 9000 Å. The second spectrum consists of 4 × 1800 s exposures taken using the *R*150 grating (*G*5306). The 1 arcsec slit provided a resolution of 22.7 Å with this grating but the useful wavelength range of the obtained spectrum increased to ∼4000–9500 Å. The SNR in the continuum was similar to the first spectrum (around 10 per pixel), albeit at lower spectral resolution.

The centroids and widths of the two strong absorption lines at around 6170 Å were measured by fitting simultaneous Gaussian profiles (see Fig. 3). This was done using our custom built IDL spectral analysis package PROCSPEC, and checked with the STARLINK spectral analysis package DIPSO. The full width at half-maximum (FWHM) was allowed to vary in tandem, and the centroids were measured at 6166.84 and 6182.15 Å. We found a best fit with FWHM = 5.4 Å which is slightly lower than the expected instrument resolution of 6.4 Å at this wavelength, for a 1 arcsec slit width. The image quality at the time of observations was lower than the slit width (around 0.7–0.8 arcsec) and the source did not completely fill the slit. The line widths are hence effectively unresolved. If these were the Mg II λλ2795.528, 2802.704[3] doublet, then the centroids both imply redshifts of $z = 1.206$. Hence this is a robust identification of the absorption components, likely in the interstellar medium (ISM) of the host galaxy of the transient. The Mg II absorber could conceivably be foreground, which would then imply an even higher redshift for the transient. We do detect a probable host galaxy, coincident with PS1-10pm in deep Gemini images after the transient has faded (see below). Although this could be a foreground or background source, the simplest explanation is that the Mg II absorption is associated with the host galaxy and the redshift of the transient PS1-10pm is the same as the Mg II absorption. In all reported cases in the literature where SLSNe Ic have detections of both Mg II absorption and host galaxy emission lines, the redshifts are the same.

Fig. 4 shows the two PS1-10pm spectra compared with spectra of SCP06F6, SN2010gx, PTF09cwl, PS1-10awh and PS1-10ky (Barbary et al. 2009; Pastorello et al. 2010a; Chomiuk et al. 2011; Quimby et al. 2011). The Mg II λλ2796, 2803 absorption doublet can be seen in most of the spectra, corrected for each respective redshift, which allowed Quimby et al. (2011) and Chomiuk et al. (2011) to determine the redshifts and luminosities of these transients. The broad absorption in PS1-10pm is almost certainly due to the same Mg II resonance transition, but in the expanding photosphere of the transient. The similarity of the depth and strength of the feature immediately suggests that PS1-10pm could be an SLSN, similar to the SLSNe Ic class illustrated here.

Fig. 3 shows a 500 Å segment of the first, R400 GMOS spectrum, corrected for the redshift obtained above. If we assume that the broad absorption line (BAL) is Mg II then the centroid is at a blueshifted velocity of ∼17 000 km s^{-1} in comparison to the Mg II ISM doublet. Chomiuk et al. (2011) find similar velocities of ∼19 000 and ∼12 000 km s^{-1} for PS1-10ky and PS1-10awh, respectively. Line widths ranging from 9000 to 12 000 km s^{-1} were found by Chomiuk et al. (2011), which are slightly less than the ∼13 000 km s^{-1} found for PS1-10pm. However, differences could arise due to the simplistic approach in fitting a FHWM to such a broad feature and ignoring possible blends. Also, we have used only the Mg II line whereas Chomiuk et al. (2011) used multiple features in the analysis of PS1-10ky and PS1-10awh.

To compare the respective absolute AB magnitude of each SN we used the following:

$$M = m - 5\log\left(\frac{d_L}{10(\rm pc)}\right) + 2.5\log(1+z) \quad (1)$$

(Hogg et al. 2002), where *m* is the apparent AB magnitude. As can be seen, the measured magnitudes were corrected for cosmological expansion but not given a full *K*-correction. However, suitable filters were chosen to make the comparison valid (see Table 8 for central wavelengths in the rest frame) with the resulting wavelength range (∼2500–4000 Å) falling approximately in the NUV. We applied a correction for foreground reddening due to the Galactic line of sight only (Schlegel, Finkbeiner & Davis 1998), as we have no information on the extinction in the host. The foreground extinction and the Cardelli, Clayton & Mathis (1989) extinction law implies $A_r \simeq 0.05$. A standard cosmology with $H_0 = 72$ km s^{-1}, $\Omega_{\rm M} = 0.27$ and $\Omega_\lambda = 0.73$ is used throughout.

Fig. 5 shows an absolute magnitude light curve of the PS1-10pm $r_{\rm P1}$ band (assuming a redshift of 1.206), along with *u*-band data for SN2010gx (Pastorello et al. 2010a) and $g_{\rm P1}$-band data for PS1-10awh and PS1-10ky (Chomiuk et al. 2011). As can be seen from Table 8, these are rest frame light curves in the NUV (∼2500–2900 Å) and they have been corrected for time dilation

[2] Gemini Program ID: GN-2010A-Q-45.
[3] http://www.nist.gov/pml/data/asd.cfm

Table 7. Observed photometry for PS1-10pm. No *K*-corrections have been applied and the phase values have not been corrected to the rest frame. Note that the PS1 observations have had any flux from a previous reference image removed through image subtraction (although note that no host object can be seen at the location of PS1-10pm) whereas the late time WHT and GN observations have not.

Date	MJD	Phase (d)	g_{P1}	r_{P1}	i_{P1}	z_{P1}	g	r	i	z	Telescope
24/12/2009	55189.65	−136.35	–	–	>23.97	–	–	–	–	–	PS1
28/12/2009	55193.65	−132.35	–	–	–	>23.03	–	–	–	–	PS1
07/01/2010	55203.61	−122.39	>23.80	>23.71	–	–	–	–	–	–	PS1
11/01/2010	55207.65	−118.35	–	–	>24.08	–	–	–	–	–	PS1
12/01/2010	55208.65	−117.35	–	–	–	>23.24	–	–	–	–	PS1
13/01/2010	55209.64	−116.36	>23.82	–	–	–	–	–	–	–	PS1
13/01/2010	55209.65	−116.35	–	>23.71	–	–	–	–	–	–	PS1
14/01/2010	55210.61	−115.39	–	–	>24.00	–	–	–	–	–	PS1
16/01/2010	55212.64	−113.36	>23.78	>23.69	–	–	–	–	–	–	PS1
17/01/2010	55213.56	−112.44	–	–	>24.11	–	–	–	–	–	PS1
18/01/2010	55214.56	−111.44	–	–	–	>23.26	–	–	–	–	PS1
19/01/2010	55215.63	−110.37	–	>23.76	–	–	–	–	–	–	PS1
23/01/2010	55219.65	−106.35	–	–	>24.02	–	–	–	–	–	PS1
24/01/2010	55220.63	−105.37	–	–	–	>23.19	–	–	–	–	PS1
25/01/2010	55221.56	−104.44	>23.78	>23.64	–	–	–	–	–	–	PS1
26/01/2010	55222.59	−103.41	–	–	>24.04	–	–	–	–	–	PS1
27/01/2010	55223.57	−102.43	–	–	–	>23.12	–	–	–	–	PS1
03/02/2010	55230.60	−95.40	>23.48	>23.47	–	–	–	–	–	–	PS1
04/02/2010	55231.58	−94.42	–	–	>23.99	–	–	–	–	–	PS1
06/02/2010	55233.53	−92.47	>23.72	>23.59	–	–	–	–	–	–	PS1
07/02/2010	55234.56	−91.44	–	–	>24.06	–	–	–	–	–	PS1
08/02/2010	55235.59	−90.41	–	–	–	>23.14	–	–	–	–	PS1
09/02/2010	55236.60	−89.40	>23.82	–	–	–	–	–	–	–	PS1
09/02/2010	55236.61	−89.39	–	>23.69	–	–	–	–	–	–	PS1
10/02/2010	55237.57	−88.43	–	–	>24.11	–	–	–	–	–	PS1
11/02/2010	55238.57	−87.43	–	–	–	>23.20	–	–	–	–	PS1
12/02/2010	55239.54	−86.46	>23.86	>23.74	–	–	–	–	–	–	PS1
13/02/2010	55240.53	−85.47	–	–	>24.07	–	–	–	–	–	PS1
15/02/2010	55242.54	−83.46	>23.85	>23.71	–	–	–	–	–	–	PS1
16/02/2010	55243.53	−82.47	–	–	>24.02	–	–	–	–	–	PS1
19/02/2010	55246.46	−79.54	–	–	>23.97	–	–	–	–	–	PS1
20/02/2010	55247.54	−78.46	–	–	–	>23.13	–	–	–	–	PS1
21/02/2010	55248.53	−77.47	>23.84	>23.71	–	–	–	–	–	–	PS1
24/02/2010	55251.51	−74.49	23.31 (0.29)	>23.47	–	–	–	–	–	–	PS1
25/02/2010	55252.55	−73.45	–	–	23.59 (0.30)	–	–	–	–	–	PS1
11/03/2010	55266.54	−59.46	23.23 (0.25)	23.68 (0.38)	–	–	–	–	–	–	PS1
13/03/2010	55268.58	−57.42	–	–	–	>22.78	–	–	–	–	PS1
17/03/2010	55272.58	−53.42	–	23.35 (0.26)	–	–	–	–	–	–	PS1
20/03/2010	55275.52	−50.48	23.16 (0.20)	23.53 (0.33)	–	–	–	–	–	–	PS1
25/03/2010	55280.35	−45.65	–	–	–	>23.20	–	–	–	–	PS1
02/04/2010	55288.44	−37.56	–	–	23.11 (0.20)	–	–	–	–	–	PS1
11/04/2010	55297.34	−28.66	–	–	22.43 (0.08)	–	–	–	–	–	PS1
12/04/2010	55298.39	−27.61	–	–	–	22.41 (0.16)	–	–	–	–	PS1
15/04/2010	55301.33	−24.67	22.93 (0.17)	22.87 (0.18)	–	–	–	–	–	–	PS1
17/04/2010	55303.49	−22.51	–	–	22.32 (0.08)	–	–	–	–	–	PS1
18/04/2010	55304.32	−21.68	–	–	–	22.34 (0.16)	–	–	–	–	PS1
19/04/2010	55305.34	−20.66	23.07 (0.21)	22.67 (0.15)	–	–	–	–	–	–	PS1
06/05/2010	55322.39	−3.61	–	–	–	21.97 (0.11)	–	–	–	–	PS1
09/05/2010	55325.37	−0.63	–	–	–	21.74 (0.09)	–	–	–	–	PS1
10/05/2010	55326.41	0.41	22.98 (0.18)	22.12 (0.10)	–	–	–	–	–	–	PS1
11/05/2010	55327.43	1.43	–	–	21.98 (0.06)	–	–	–	–	–	PS1
13/05/2010	55329.37	3.37	23.13 (0.18)	22.22 (0.09)	–	–	–	–	–	–	PS1
14/05/2010	55330.30	4.30	–	–	22.02 (0.06)	–	–	–	–	–	PS1
16/05/2010	55332.31	6.31	23.41 (0.22)	22.33 (0.09)	–	–	–	–	–	–	PS1
18/05/2010	55334.33	8.33	–	–	–	21.79 (0.09)	–	–	–	–	PS1
23/05/2010	55339.28	13.28	–	–	21.63 (0.08)	–	–	–	–	–	PS1
24/05/2010	55340.28	14.28	–	–	–	21.98 (0.14)	–	–	–	–	PS1
01/06/2010	55348.34	22.34	–	–	22.06 (0.06)	–	–	–	–	–	PS1
03/06/2010	55350.30	24.30	23.66 (0.28)	22.42 (0.10)	–	–	–	–	–	–	PS1
05/06/2010	55352.33	26.33	–	–	–	21.68 (0.08)	–	–	–	–	PS1
06/06/2010	55353.35	27.35	23.56 (0.29)	22.80 (0.17)	–	–	–	–	–	–	PS1

Table 7 – *continued*

Date	MJD	Phase (d)	g_{P1}	r_{P1}	i_{P1}	z_{P1}	g	r	i	z	Telescope
07/06/2010	55354.26	28.26	–	–	22.31 (0.08)	–	–	–	–	–	PS1
08/06/2010	55355.26	29.26	–	–	–	21.70 (0.12)	–	–	–	–	PS1
12/06/2010	55359.31	33.31	–	22.72 (0.26)	–	–	–	–	–	–	PS1
13/06/2010	55360.26	34.26	–	–	22.21 (0.08)	–	–	–	–	–	PS1
14/06/2010	55361.26	35.26	–	–	–	21.94 (0.12)	–	–	–	–	PS1
15/06/2010	55362.28	36.28	–	22.66 (0.13)	–	–	–	–	–	–	PS1
16/06/2010	55363.27	37.27	–	–	22.22 (0.07)	–	–	–	–	–	PS1
17/06/2010	55364.26	38.26	–	–	–	22.08 (0.12)	–	–	–	–	PS1
18/06/2010	55365.28	39.28	–	22.72 (0.15)	–	–	–	–	–	–	PS1
19/06/2010	55366.27	40.27	–	–	22.36 (0.09)	–	–	–	–	–	PS1
20/06/2010	55367.26	41.26	–	–	–	21.89 (0.10)	–	–	–	–	PS1
06/07/2010	55383.97	57.97	–	–	–	–	–	23.52 (0.13)	22.65 (0.23)	–	WHT
07/07/2010	55384.00	58.00	–	–	–	–	24.82 (0.33)	–	–	22.16 (0.28)	WHT
30/01/2011	55591.62	265.62	–	–	–	–	–	–	24.99 (0.42)	24.86 (0.31)	GN

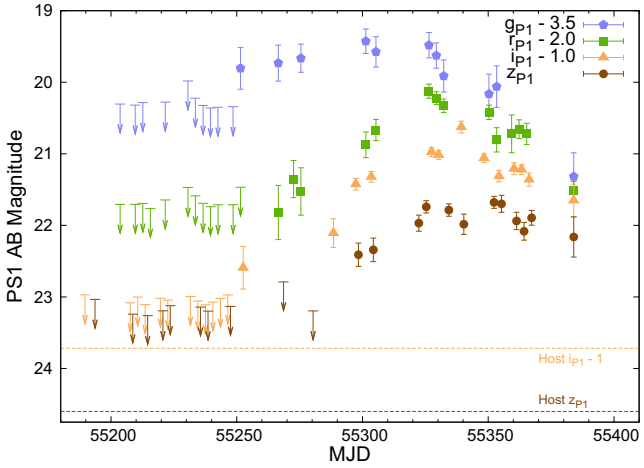

Figure 2. Observed $griz_{P1}$ light curves of PS1-10pm. The non-PS1, WHT detections are the *griz* points shown at MJD 55384 and any upper limits are marked with arrows. Measurements of the host galaxy from late-time, deep GN *i*- and *z*-band images are shown as horizontal lines. During the 2011 season, between MJD 55594.56 and 55736.33, there have been 10 non-detections in g_{P1} down to a 3σ indicative magnitude limit of 23.89, 12 non-detections in r_{P1} down to 23.90, 12 non-detections in i_{P1} down to 24.10 and 10 non-detections in z_{P1} down to a limit of 23.24. Over the entire course of the observations there are also 24 non-detections in y_{P1}, however given that the limiting magnitude for this filter only reached a maximum magnitude of 21.86, observations of an object at the redshift of PS1-10pm were unfeasible.

for the figure. PS1-10pm reached a peak absolute magnitude $M_{NUV} = -21.59 \pm 0.07$ after a rise time lasting ∼35 d. The similarities in the light-curve shapes further supports the classification of PS1-10pm as an SLSN Ic, but at one of the highest known redshifts of $z = 1.206$. Two further light curves, obtained from *u*-band PTF12dam data (Nicholl et al. 2013) and g_{P1}-band PS1-11ap data (McCrum et al. 2014), are also presented in this figure, showing a clear distinction between these slowly evolving, SLSNe Ic and the normal SLSNe Ic class. The light curves for the former are much broader and easily distinguishable.

Chomiuk et al. (2011) and Inserra et al. (2013) showed that the colour and luminosity evolution of these SLSNe Ic are physically consistent with hot blackbody temperatures ranging from $T_{eff} \sim 20\,000$ K at 20 d before peak through $T_{eff} \sim 15000$ K at peak luminosity. Hence we can use the well-sampled PS1 multicolour light curve to trace the blackbody temperature of PS1-10pm to check for consistency with the known population of these transients. The PS1 bandpasses probe the rest-frame NUV wavelengths 2200–4000 Å for PS1-10pm and although this is a rather narrow window for a spectral energy distribution (SED) it is well suited to the high photospheric temperatures. We chose to determine a blackbody fit at five epochs which had approximately simultaneous and consistent *griz* coverage (see Table 9), giving a range between −20 and +30 d with respect to peak. The fits and temperatures are shown in Fig. 6, which illustrate a physically consistent evolution of temperature which is similar to the lower redshift SLSNe Ic as shown in fig. 8 of Chomiuk et al. (2011). At peak luminosity, a temperature of $T_{eff} \sim 10\,000$ provides a blackbody spectrum fit to the flux of PS1-10pm. This gives an integrated luminosity (between 1000 and 10 000 Å) of $\sim 3 \times 10^{44}$ erg s^{-1}, or 7.3×10^{10} L$_\odot$. This is again very similar to the SLSNe Ic in Quimby et al. (2011), Pastorello et al. (2010a) and Chomiuk et al. (2011). The radius of the emitting surface must then be of the of order 6×10^{15} cm, which is a factor of 2 larger than previously determined by Chomiuk et al. (2011) for PS1-10awh and PS1-10aky, due to the lower peak T_{eff} that we determine. However, within the intrinsic uncertainties of the assumptions of blackbody radiation, the narrow spectral energy range and flux measurements, we cannot say if this is real diversity or limitations of the fairly simple physics we employ. In conclusion, the PS1 measured multicolour light curve is physically consistent with PS1-10pm being an SLSN Ic at $z = 1.206$. The spectrum in Fig. 4 illustrates the difficulties in classifying high-*z* SN candidates from optical spectra. At $z > 1$, one typically gets a region of the rest-frame UV that is a factor of 2 smaller in wavelength coverage than the observer frame spectrum. The lack of large numbers of SNe (particularly unusually luminous SNe which will be preferentially detected at high-*z*) with rest-frame UV spectra often makes the classification and redshift determination difficult.

4.2 Host galaxy of PS1-10pm

We obtained deep images in *i* and *z* at the position of PS1-10pm with 9 × 150 s exposures at GN, ∼265 d after the i_{P1}-band peak. The data were reduced as normal by subtracting a bias level gleaned from the overscan region of the Gemini CCD, dividing each image by an appropriate flat-field image and subtracting an appropriately scaled, sourceless fringe frame created using the *gifringe* function

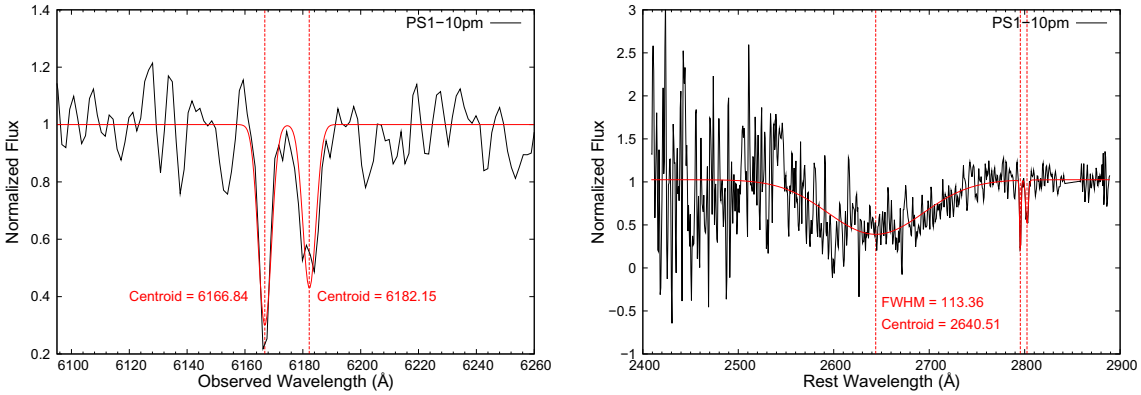

Figure 3. Detail of the GMOS, R400 PS1-10pm spectrum showing the observed wavelength of the two absorption features thought to be the Mg II λλ2796, 2803 doublet used to determine a redshift of 1.206. By taking the narrow doublet (seen here at the observed wavelength in the left-hand figure and at the implied rest wavelength of ∼2800 Å in the right-hand figure) to be Mg II in the host galaxy and thus using it as a rest frame for the wider, bluer profile from the SN, simple Gaussian profiles could be fitted to the absorption profiles and an expansion velocity of ∼17 000 km s^{-1} determined for PS1-10pm.

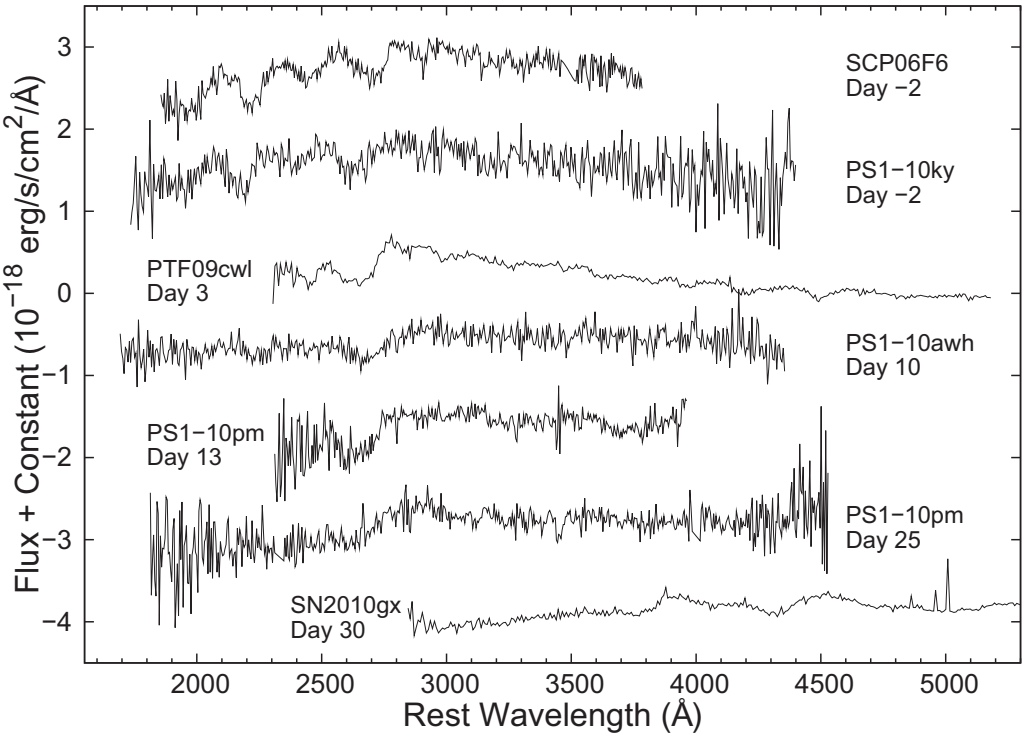

Figure 4. Two GMOS spectra of PS1-10pm at $z = 1.206$ compared with PS1-10awh at $z = 0.908$, PS1-10ky at $z = 0.956$, PTF09cwl at $z = 0.349$, SCP06F6 at $z = 1.189$ and SN2010gx at $z = 0.23$ (see references in the text). All of the spectra have been corrected to rest frame and rebinned to 10 Å and some chip gaps have been smoothed over.

Table 8. Central rest wavelengths (Å) of optical passbands for each of the SLSNe Ic used in the photometric comparisons in this paper, where values in *italic* represent filters used for comparison purposes. The redshift of each object is given in the top row and the central wavelength of each filter in the second column.

Filter		PS1-10pm	PS1-10ahf	PS1-10awh	PS1-10ky	SN 2010gx	PS1-11ap	PTF12dam
		1.206	1.1	0.908	0.956	0.230	0.524	0.107
u	3540	–	–	–	–	*2878*	–	*3196*
g	4860	2206	2256	*2550*	*2488*	3878	*3193*	*4396*
r	6230	*2826*	*2890*	3267	3188	5065	*4091*	5632
i	7525	3412	3489	3944	3848	6199	4939	6799
z	8660	3924	*4012*	4536	4426	7426	5680	7820
y	9720	4409	4508	5097	4974	–	6382	8786

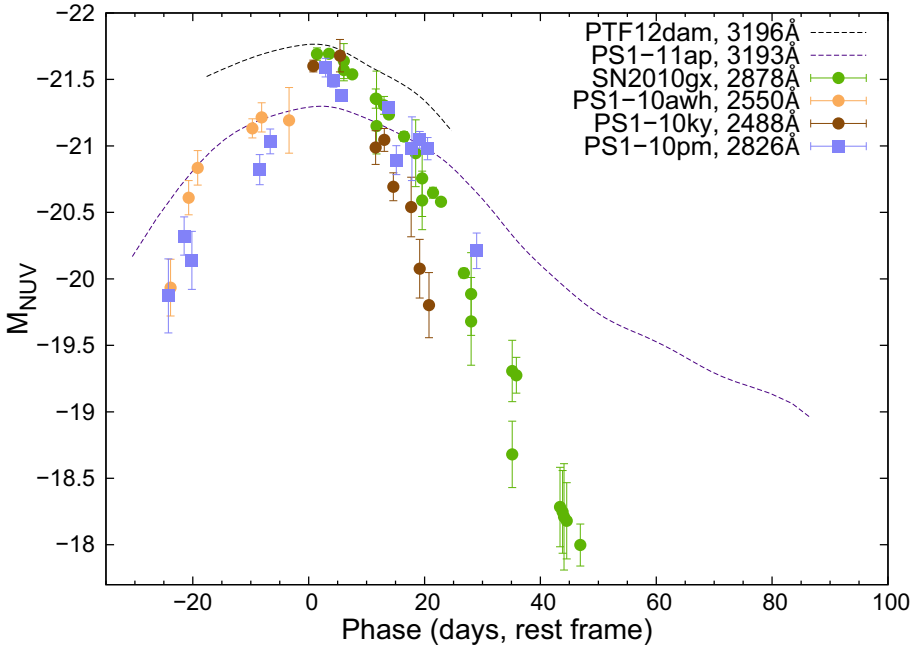

Figure 5. A comparison of the PS1-10pm r_{P1}-band absolute magnitude light curve with a u-band SN2010gx light curve and g_{P1}-band PS1-10awh and PS1-10ky light curves. Light-curve shapes obtained from u-band PTF12dam and g_{P1}-band PS1-11ap data are also presented here, highlighting the difference in the evolution of the SLSNe Ic data set. The rest wavelengths of these bands for each object are given in Table 8 and the comparison here approximately represents the NUV, with a range of ∼2500–3200 Å.

Table 9. PS1-10pm estimated temperatures from blackbody fitting.

MJD	Phase (d, rest)	T_{BB} (K)
∼55283	−20	20000 ± 5000
∼55305	−8	12500 ± 2500
∼55325	0	10000 ± 1000
∼55367	20	7500 ± 1000
∼55384	30	6000 ± 1000

in the *gemini* IRAF[4] package. Although no host was seen in the PS1 reference templates, a faint object can be seen in the deeper Gemini images. Aperture photometry was carried out using the aperture photometry procedure available in the Graphical Astronomy and Image Analysis tool software package[5] (GAIA; Draper et al. 2009), giving an i-band magnitude of $i = 24.99 \pm 0.42$ and an observed z-band magnitude of $z = 24.86 \pm 0.31$. These correspond to absolute magnitude values of $M_{3400} \sim -18.7$ and $M_{3900} \sim -18.9$, respectively, when corrected to $z = 1.206$ and for foreground extinction.

The position of an SN with respect to its host galaxy can provide evidence against it being misclassified as an AGN, provided an offset from the galactic centre is found. Alignment of the GN i-band image with a PS1 i_{P1}-band image of the SLSN Ic at peak was carried out by first measuring the pixel coordinates of 10 bright stars in a 6.5 arcmin × 2.8 arcmin field using the IRAF *phot* task utilizing the centroid centring algorithm on both images. The list of matched coordinates was then used as an input to the IRAF *geomap* task to derive a geometric transformation between the two images, allowing for translation, rotation and independent scaling in the x- and y-axes. The rms of the fit was 0.061 arcsec (GMOS pixels are 0.1454 arcsec and PS1 GPC pixels are 0.25 arcsec after warping).

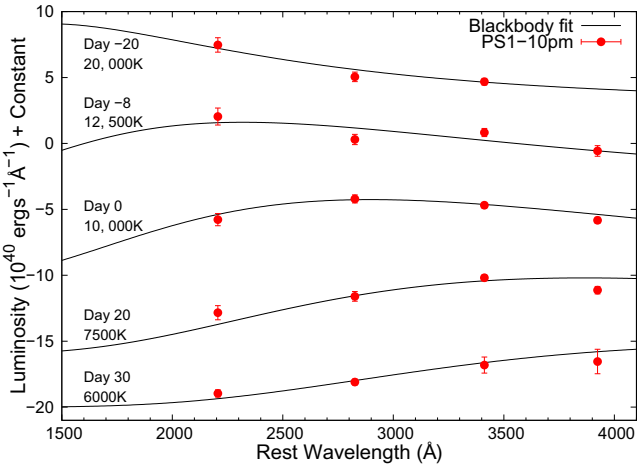

Figure 6. Blackbody fitting of PS1-10pm across five epochs.

Aperture photometry was then carried out on the host galaxy (in the Gemini image) and PS1-10pm (in the original PS1 image). The coordinates of the SLSN Ic and of the host galaxy were measured in both images with three different centring algorithms provided by the *phot* task; centroid, Gaussian and optimal filtering. This provided a mean position and a standard deviation. The standard deviation of the three measurements was taken as the positional error measurement in x and y of the two objects.

The x, y position of PS1-10pm was then transformed to the coordinate system of the GMOS frame using the transformation defined by the 10 stars in common. This revealed a difference of 2.24 GMOS

[4] IRAF is distributed by the National Optical Astronomy Observatories, which are operated by the Association of Universities for Research in Astronomy, Inc., under the cooperative agreement with the National Science Foundation.
[5] http://astro.dur.ac.uk/∼pdraper/gaia/gaia.html

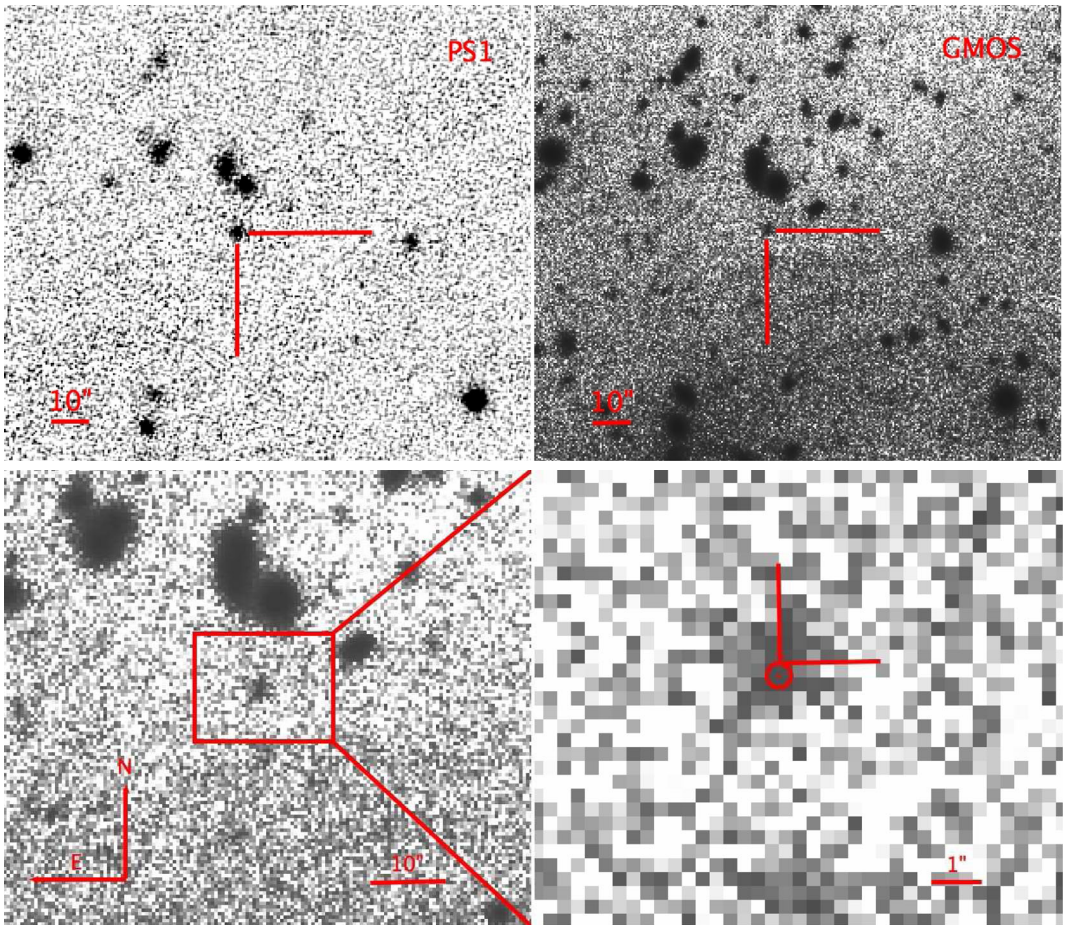

Figure 7. PS1 and GN i_{P1}- and i-band images of the SLSN Ic PS1-10pm at peak and after the explosion has faded. The lower set of images show subsections of the host galaxy of PS1-10pm, 265 d after peak. The circle in the zoomed, lower-right image is centred on the SLSN Ic position with a radius corresponding to 3σ. The perpendicular lines in this image meet at the determined centroid of the galaxy which can be seen to be just inside the 3σ boundary of the SLSN Ic position.

pixels which, at the 0.1454 arcsec resolution of GN (for a 2 × 2 binned CCD with a pixel scale of 0.0727 arcsec pixel^{-1})[6] corresponds to an offset of 0.33 arcsec (see Fig. 7).

The total uncertainty in the alignment of the two objects is hence the quadrature sum of the uncertainties in the centroids of the host and PS1-10pm and the rms of the alignment transformation (see e.g. Smartt et al. 2004). This was found to be $\sigma = 0.806$ pixels (or 0.12 arcsec) and hence the SLSN Ic and the galaxy centroid differ by 2.8σ. While this is not quite a formal 3σ difference, it indicates that the SN is not coincident with the centre of the galaxy, hence supports evidence that PS1-10pm is an SLSN and is not a UV transient event due to any type of AGN variability.

Lunnan et al. (2014) have shown that the host of PS1-10pm actually breaks up into a resolved source which is significantly extended and has an irregular morphology in *Hubble Space Telescope* images. They determine AB magnitudes of $m_{F606W} = 25.38 \pm 0.05$ and $m_{F110W} = 24.40 \pm 0.08$. Our i- and z-band filter mag sit comfortably between these mag, which would allow four points on the SED to be used for future analysis.

[6] http://www.gemini.edu/sciops/instruments/gmos/imaging/detector-array/gmosn-array-eev

4.3 PS1-10ahf

PS1-10ahf was first detected on MJD 55414 (2010 August 6) in MD10 at RA = $23^h32^m28^s.3$, Dec. = $-00°21'43''.6$. The initial light curve of PS1-10ahf showed a faint, slowly rising source clearly detected in the i_{P1} and z_{P1} bands ($i_{P1} \sim 23.3$). PS1 followed the field until MJD 55535 (2010 December 5), thereafter the field was dropped from the PS1 observing cycle due to airmass constraints. The details of these observations can be found in Table 10. No sign of a host was found in any of the major survey catalogues, nor was it visible in the PS1 reference stack images. As a check, manual photometry was also carried out independently of both the automated pipelines described in Section 2.2. The optimal photometry facility within GAIA was again used to perform photometry on the target images rather than the difference images. As there was clearly no host contribution in the PS1 reference stack image, there should not be any contribution to the luminosity other than that of the transient. The manual light curves for the i_{P1} and z_{P1} bands were calibrated using eight SDSS stars in the field of the transient, and in all cases the photometry was consistent with the pipeline measurements. The epoch of the i_{P1}-band maximum was found from a second order polynomial fit and determined to be MJD 55540 ± 5. Observed r_{P1}-, i_{P1}- and z_{P1}-band light curves for PS1-10ahf can be found in Fig. 8.

Table 10. Observed photometry for PS1-10ahf. No *K*-corrections have been applied. Phase is in observer frame, not rest frame, as more than one possible redshift value is presented in the text. Note that the PS1 observations have had any flux from previous reference image removed through image subtraction (although note that no host object can be seen at the location of PS1-10ahf) whereas the late time WHT and GS observations have not.

Date	MJD	Phase (d)	r_{P1}	i_{P1}	z_{P1}	r	i	z	Telescope
11/07/2010	55388.59	− 151.41	–	–	>23.89	–	–	–	PS1
12/07/2010	55389.52	− 150.48	>24.37	–	–	–	–	–	PS1
21/07/2010	55398.61	− 141.39	>23.69	–	–	–	–	–	PS1
02/08/2010	55410.55	− 129.45	>23.80	–	–	–	–	–	PS1
04/08/2010	55412.55	− 127.45	–	–	23.98 (0.31)	–	–	–	PS1
05/08/2010	55413.54	− 126.46	23.77 (0.19)	–	–	–	–	–	PS1
08/08/2010	55416.56	− 123.44	24.42 (0.28)	–	–	–	–	–	PS1
09/08/2010	55417.56	− 122.44	–	23.16 (0.09)	–	–	–	–	PS1
14/08/2010	55422.56	− 117.44	>23.99	–	–	–	–	–	PS1
15/08/2010	55423.56	− 116.44	–	23.00 (0.06)	–	–	–	–	PS1
16/08/2010	55424.57	− 115.43	–	–	>23.68	–	–	–	PS1
17/08/2010	55425.56	− 114.44	>24.27	–	–	–	–	–	PS1
19/08/2010	55427.57	− 112.43	–	–	23.85 (0.23)	–	–	–	PS1
20/08/2010	55428.56	− 111.44	23.94 (0.24)	–	–	–	–	–	PS1
30/08/2010	55438.58	− 101.42	–	23.08 (0.10)	–	–	–	–	PS1
31/08/2010	55439.54	− 100.46	–	–	22.96 (0.12)	–	–	–	PS1
01/09/2010	55440.53	− 99.47	23.65 (0.24)	–	–	–	–	–	PS1
02/09/2010	55441.52	− 98.48	–	22.94 (0.07)	–	–	–	–	PS1
03/09/2010	55442.57	− 97.43	–	–	23.41 (0.28)	–	–	–	PS1
04/09/2010	55443.50	− 96.5	23.41 (0.14)	–	–	–	–	–	PS1
05/09/2010	55444.48	− 95.52	–	22.88 (0.06)	–	–	–	–	PS1
06/09/2010	55445.52	− 94.48	–	–	23.39 (0.24)	–	–	–	PS1
07/09/2010	55446.55	− 93.45	23.65 (0.18)	–	–	–	–	–	PS1
08/09/2010	55447.53	− 92.47	–	22.72 (0.06)	–	–	–	–	PS1
09/09/2010	55448.47	− 91.53	–	–	23.29 (0.13)	–	–	–	PS1
10/09/2010	55449.51	− 90.49	–	–	–	–	–	–	PS1
12/09/2010	55451.51	− 88.49	–	–	>23.29	–	–	–	PS1
13/09/2010	55452.43	− 87.57	23.40 (0.13)	–	–	–	–	–	PS1
14/09/2010	55453.46	− 86.54	–	22.75 (0.05)	–	–	–	–	PS1
17/09/2010	55456.45	− 83.55	–	22.64 (0.04)	–	–	–	–	PS1
18/09/2010	55457.35	− 82.65	–	–	22.86 (0.19)	–	–	–	PS1
19/09/2010	55458.33	− 81.67	–	–	–	–	–	–	PS1
26/09/2010	55465.52	− 74.48	–	22.56 (0.12)	–	–	–	–	PS1
27/09/2010	55466.41	− 73.59	–	–	22.56 (0.09)	–	–	–	PS1
28/09/2010	55467.43	− 72.57	23.28 (0.22)	–	–	–	–	–	PS1
06/10/2010	55475.27	− 64.73	–	–	22.45 (0.10)	–	–	–	PS1
07/10/2010	55476.45	− 63.55	22.76 (0.10)	–	–	–	–	–	PS1
08/10/2010	55477.27	− 62.73	–	22.62 (0.04)	–	–	–	–	PS1
09/10/2010	55478.26	− 61.74	–	–	22.82 (0.10)	–	–	–	PS1
10/10/2010	55479.27	− 60.73	23.45 (0.21)	–	–	–	–	–	PS1
11/10/2010	55480.36	− 59.64	–	22.62 (0.06)	–	–	–	–	PS1
12/10/2010	55481.29	− 58.71	–	–	22.75 (0.13)	–	–	–	PS1
13/10/2010	55482.27	− 57.73	23.25 (0.19)	–	–	–	–	–	PS1
14/10/2010	55483.26	− 56.74	–	22.51 (0.04)	–	–	–	–	PS1
15/10/2010	55484.24	− 55.76	–	–	22.59 (0.09)	–	–	–	PS1
16/10/2010	55485.26	− 54.74	22.93 (0.16)	–	–	–	–	–	PS1
29/10/2010	55498.26	− 41.74	–	22.56 (0.05)	–	–	–	–	PS1
30/10/2010	55499.26	− 40.74	–	–	22.45 (0.10)	–	–	–	PS1
31/10/2010	55500.05	− 39.95	–	–	–	–	22.60 (0.14)	–	WHT
31/10/2010	55500.26	− 39.74	22.95 (0.07)	–	–	–	–	–	PS1
01/11/2010	55501.39	− 38.61	–	22.63 (0.08)	–	–	–	–	PS1
02/11/2010	55502.30	− 37.7	–	–	22.63 (0.09)	–	–	–	PS1
03/11/2010	55503.34	− 36.66	23.17 (0.11)	–	–	–	–	–	PS1
04/11/2010	55504.41	− 35.59	–	22.74 (0.09)	–	–	–	–	PS1
07/11/2010	55507.33	− 32.67	–	22.56 (0.06)	–	–	–	–	PS1
08/11/2010	55508.25	− 31.75	–	–	22.57 (0.12)	–	–	–	PS1
10/11/2010	55510.31	− 29.69	–	22.52 (0.05)	–	–	–	–	PS1
30/11/2010	55530.33	− 9.67	–	–	–	–	–	–	PS1

Table 10 – *continued*

Date	MJD	Phase (d)	r_{P1}	i_{P1}	z_{P1}	r	i	z	Telescope
04/12/2010	55534.30	−5.7	–	22.52 (0.09)	–	–	–	–	PS1
05/12/2010	55535.24	−4.76	–	–	22.28 (0.07)	–	–	–	PS1
06/12/2010	55536.27	−3.73	22.76 (0.12)	–	–	–	–	–	PS1
24/07/2011	55766	226.0	–	–	–	24.52 (0.06)	–	–	GS
26/07/2011	55768	228.0	–	–	–	–	–	23.80 (0.10)	GS
08/08/2011	55781.14	241.14	–	–	–	–	24.17 (0.07)	–	WHT

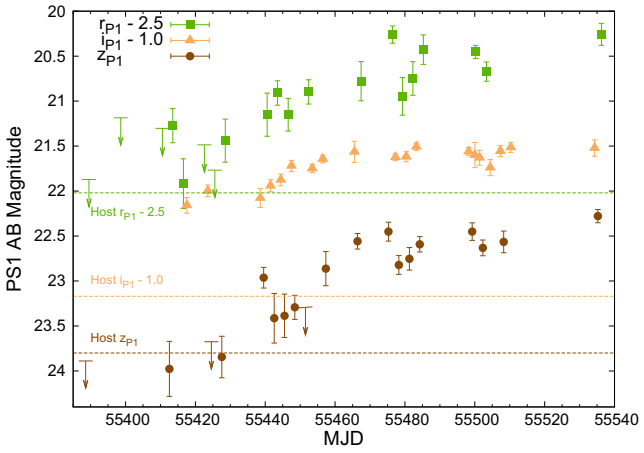

Figure 8. Observed r_{P1}-, i_{P1}- and z_{P1}-band light curves of PS1-10ahf. Measurements of the host galaxy from a deep, WHT i-band observation and deep, GS r- and z-band images are shown as horizontal lines and any upper limits are indicated with arrows. During this period, from MJD 55389.54 until 55530.33, 20 non-detections in g_{P1} are also recorded down to a photometric limit of 24.59 and a g-band limit of ∼27 is found for the host from a deep, GS g-band observation.

A spectrum of PS1-10ahf was obtained with GMOS on GS[7] on the 2010 November 6 using the $R150$ grating ($G5306$) with a 1 arcsec slit, giving a useful wavelength range from ∼4300 to 8000 Å. A set of 4 × 2700 s exposures gave a combined SNR of ∼19 in the continuum, when rebinned to 10 Å per pixel. The flux calibrated GMOS spectrum provides a synthetic r_{P1}-band magnitude of 22.8 as calculated in SYNPHOT. This flux (on 2010 November 06) is in reasonable agreement (within ±0.2 mag) of the PS1 photometry. The synthetic g_{P1}-band magnitude from the same spectrum of 24.7 is consistent with the non-detection in the nightly PS1 images. There are no strong and obvious narrow features either in absorption (e.g. Mg II or Ca II ISM lines) or in emission (e.g. nebular lines) to provide an unambiguous redshift. Hence, we initially compared it to a range of SNe, including the SLSNe Ic that we used for the PS1-10pm comparison and the confirmed $z \simeq 1$ SLSNe Ic already from PS1 (Chomiuk et al. 2011). There are a number of broad absorption or P-Cygni features, and a plausible redshift of $z = 1.1$ would put the deepest absorption at a rest wavelength similar to the broad Mg II absorption seen in other SLSNe Ic (Fig. 9). However, the spectrum lacks C II and Si II as detected in previous SLSNe Ic (Chomiuk et al. 2011; Quimby et al. 2011) and overall is not an entirely convincing match. Attempts to match the PS1-10ahf spectrum with other features typical of SNe Ic, such as Ca II H&K features and some Fe II blends, also proved unconvincing.

[7] Gemini Program ID: GS-2010B-Q-43.

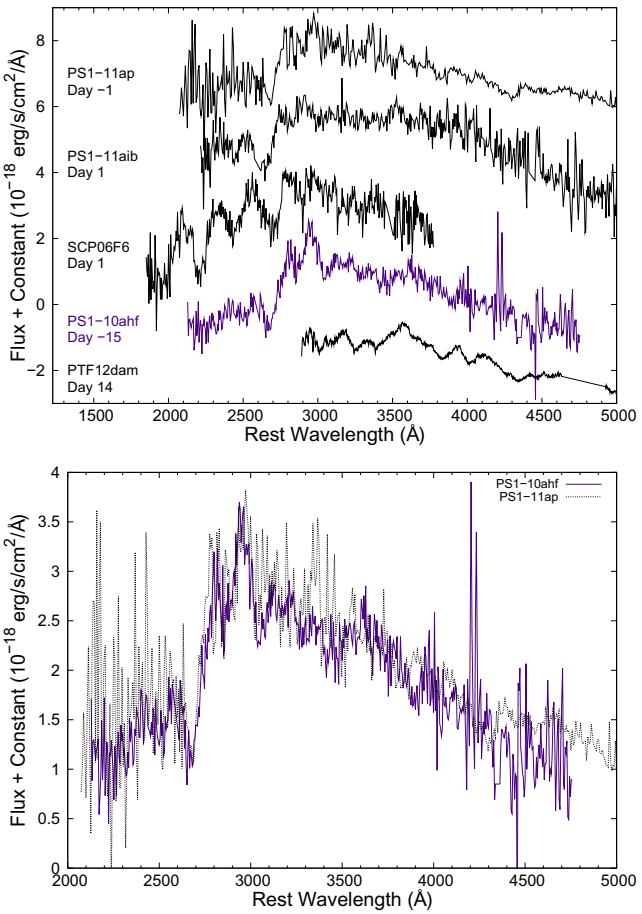

Figure 9. GMOS spectrum of PS1-10ahf at $z = 1.1$, taken with GS, compared with PS1-11ap at $z = 0.524$, PS1-11aib at $z = 0.997$, SCP06F6 at $z = 1.189$ and PTF12dam at $z = 0.108$. The lower plot shows an overlay of the PS1-10ahf spectrum with the same PS1-11ap spectrum as in the top panel to emphasize the similarities between the objects. All of the spectra have been rebinned to 10 Å and some chip gaps have been smoothed over. See references in the text.

Fig. 10 shows a comparison of an absolute magnitude r_{P1}-band PS1-10ahf light curve with u-band data for SN2010gx (Pastorello et al. 2010a), g_{P1}-band data for PS1-10awh and PS1-10ky (Chomiuk et al. 2011) and r_{P1}-band PS1-10pm data (this paper), again created using equation (1). The central wavelengths in the rest frame for these filters offer a reliable comparison as shown in Table 8. The measured magnitudes were corrected for cosmological expansion and foreground reddening for Galactic line of sight only (Schlegel et al. 1998) as again we have no host extinction information. The foreground extinction and the Cardelli et al. (1989) extinction law implies $A_i \simeq 0.07$. The long rise time of PS1-10ahf is still prevalent

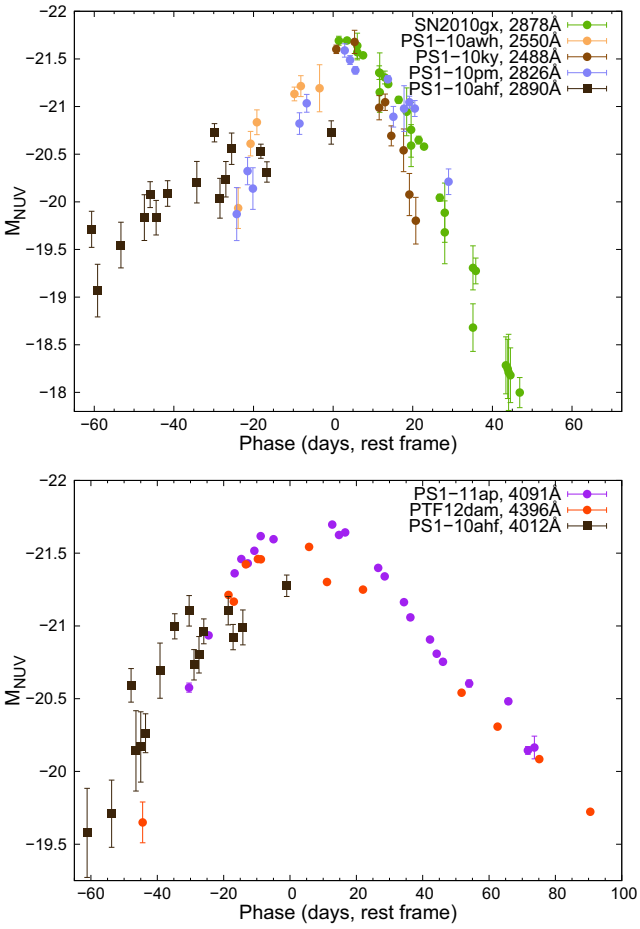

Figure 10. A variation on Fig. 5, again showing an absolute u-band SN2010gx light curve, absolute g_{P1}-band PS1-10awh and PS1-10ky light curves and an absolute r_{P1}-band PS1-10pm light curve. An absolute r_{P1}-band light curve of PS1-10ahf is shown here for comparison purposes, with $z = 1.1$. The lower image offers a comparison of a z_{P1}-band light curve of PS1-10ahf with r_{P1}-band PS1-11ap and g-band PTF12dam data. See references within.

after correcting for time dilation and clearly sets the transient apart from the normal SLSNe Ic class.

If this redshift of $z = 1.1$ from the spectral comparisons is secure then the transient is a closer match to the slowly evolving SLSNe Ic PS1-11ap (McCrum et al. 2014) and PTF12dam (Nicholl et al. 2013), as seen in the lower plot in Fig. 10. PS1-11ap has broad Mg II absorption with a line width of $\sim$14 500 km s^{-1}. The line width of possible Mg II absorption was determined to be $\sim$12 000 km s^{-1} for PS1-10ahf which compares well to PS1-11ap (see lower plot in Fig. 9). The overall spectral match to PS1-11ap was the closest we could find, after comparing with all known types of SNe for which NUV spectra exist. At this redshift the light curve is very broad, even after applying time dilation. The transient has an intrinsically slow rest-frame rise of 60 d in the NUV bands (see Fig. 10). The rising slope, within the photometric uncertainties is similar to 45–60 d rise time deduced from the modelling of PS1-11ap (McCrum et al. 2014). Unfortunately, we do not sample the decay time after peak for PS1-10ahf, simply due to the length of the PS1 observing season.

The plots show a peak absolute magnitude $M_{NUV} = -21.39 \pm 0.07$ for PS1-10ahf however the polynomial fit used to determine the peak MJD suggests that the transient continued to brighten for a short time after the observing period had ended. This illustrates a practical limitation in following the evolution of transients with broad light curves and slow evolution times combined with time dilation at $z > 1$. A typical PS1 observing season for a MD field is 150–180 d, meaning that a transient at $z \sim 1$ with a symmetric light curve and rise time of 40 d (rest frame) needs to be discovered close to the start of the observing season for the MD field if one is to sample the full rise and decay time. We were fortunate that this occurred for PS1-11ap (at $z = 0.524$; McCrum et al. 2014). In conclusion, we find the most likely match to the light curve and spectrum of PS1-10ahf is with the slowly evolving SLSNe Ic PS1-11ap. To further illustrate the connection we show a spectrum of PS1-11aib. The latter transient fell outside the survey window set for this paper (discovered on the 2011 July 27 in MD09), but it too has a broad, red light curve and a spectrum with very similar absorption features and slope to both PS1-10ahf and PS1-11ap. PS1-11aib has a convincing detection of Mg II λλ2796, 2803 ISM doublet at a redshift of $z = 0.997$ and will be discussed in a future PS1 paper (Lunnan et al., in preparation). Unfortunately, due to the high redshift of PS1-10ahf, a direct comparison with other published objects of this class (SN2007bi and PTF12dam) is not possible as the rest wavelength ranges do not have a sufficient overlap. A PTF12dam spectrum is included for completeness but, as can be seen in Fig. 9, the main features of the PS1-10ahf spectrum fall just bluewards of the reach of PTF12dam. Nevertheless, as is exemplified in the lower plot of Fig. 9, the continuum shape of the PS1-10ahf spectrum and the slowly evolving SLSNe Ic spectra are very similar.

4.4 Was PS1-10ahf a variable BAL QSO?

Initial difficulties in determining any spectral features in the PS1-10ahf GMOS spectrum led us to consider if the object was perhaps a BAL quasar (QSO). Fig. 11 shows a PS1-10ahf spectrum at rest wavelength compared with FeLoBal SDSS 1730+5850, 1154+0300, 0300+0048 and 0819+4209 (Hall et al. 2002) with the redshift of PS1-10ahf set at $z = 1.07$. These BAL QSOs can show absorption troughs $\sim$2000–20 000 km s^{-1} arising from gas with blueshifted velocities up to 66 000 km s^{-1} (Foltz et al. 1983) giving broad spectral features that can be comparable to typical SNe features in low to moderate SNR spectra. A number of other features (possibly Fe II and Ca II, most apparent in SDSS 0300+0048) in the QSO spectra match shallower absorption features in PS1-10ahf. However, there is no convincing match to any of these, particularly as the spectral break in the QSOs due to broad Mg II absorption is much deeper in the QSOs compared to PS1-10ahf. In Fig. 11, we show the QSO spectra compared with PS1-10ahf. We matched the flux level in the rest-frame continuum region 2200–2700 Å of each object to show the contrast in the spectrum break expected if PS1-10ahf was a BAL QSO. In all cases, the BAL QSO spectral breaks are significantly larger than that of PS1-10ahf and it seems unlikely that they can be similar objects. While any underlying galaxy flux might be expected to dilute the transient flux of PS1-10ahf, and hence increase the spectral break, the host galaxy is at least 2 mag fainter than the transient when the spectrum was taken (see Table 10). Therefore, flux dilution cannot account for the differences. In addition, the unusual QSOs of the Hall et al. (2002) sample are significantly more luminous than PS1-10ahf (if the latter is at $z = 1.07$), as they range between $M_{NUV} \sim -23$ and -29, compared to $M_{NUV} \simeq -21$ for PS-10ahf.

We carried out a similar search for the host galaxy of PS1-10ahf as for PS1-10pm to align it with the position of the transient. A

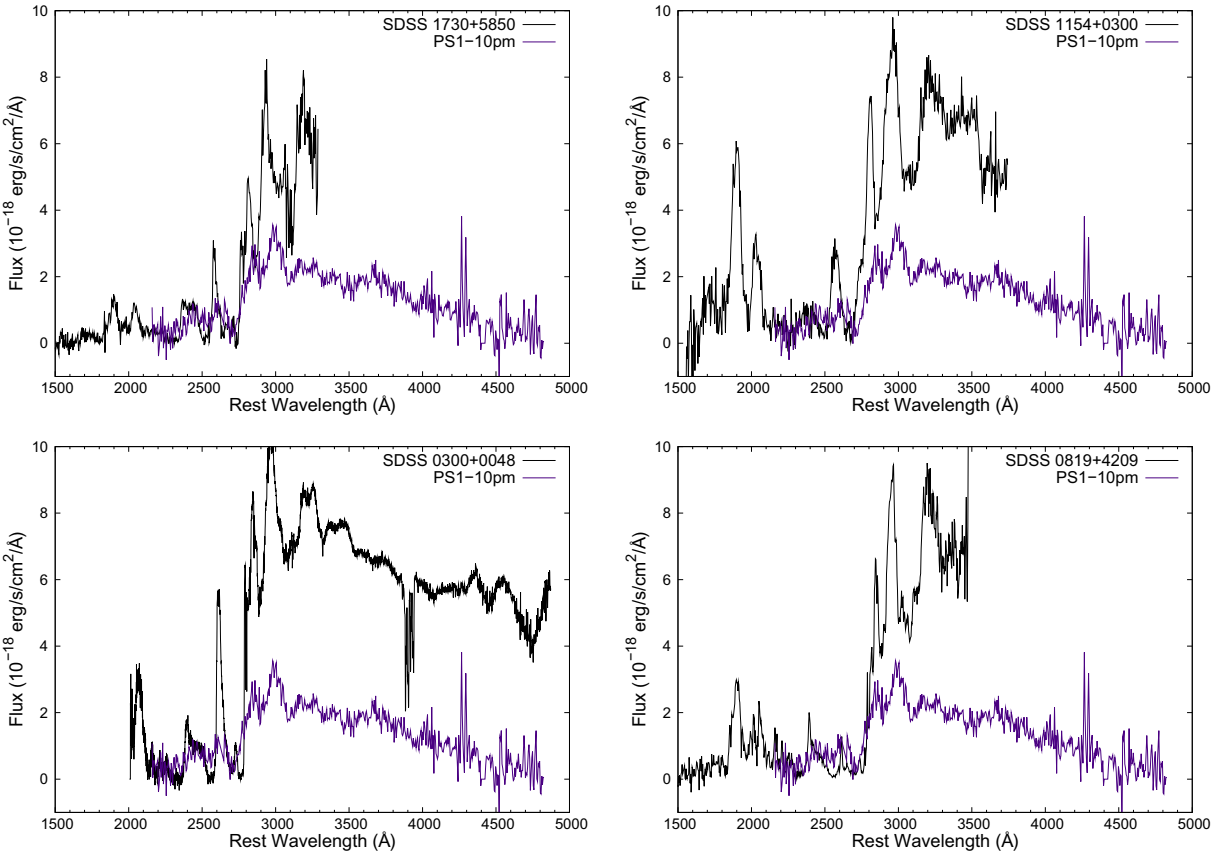

Figure 11. A comparison of PS1-10ahf with the SDSS quasars 1730+5850 ($z = 2.035$), 1154+0300 ($z = 1.458$), SDSS 0300+0048 ($z = 0.892$) and 0819+4209 ($z = 1.926$) where $z = 1.07$ for PS1-10ahf. All of the spectra have been rebinned to 10 Å and some chip gaps have been smoothed over. See references in the text.

deep i image was obtained with a 600 s exposure using the ACAM instrument on the WHT, 241 d after the determined peak epoch. The data were reduced by subtracting a separate bias image and dividing the image by an appropriate flat-field image, taken on the same night. As can be seen in Fig. 12 an object can clearly be seen at the expected coordinates and an observed i-band magnitude of $i = 24.17 \pm 0.07$ was determined using the photometry procedures available in the GAIA software package (Draper et al. 2009). Taking $z = 1.1$ and $A_i = 0.07$ gives an absolute magnitude of $M_{3400} \sim -19.5$. Note that a point source was again chosen as a reference PSF for the galaxy however, due to high redshift involved, the target appears approximately point-like. As before, both optimal and aperture photometry procedures were carried out to ensure that this approach was sensible.

Alignment of the WHT i-band image with a PS1 $i_{\rm P1}$-band image of the transient at peak was carried out using the method described in Section 4.2. The coordinates of 10 bright stars in a 6.5 arcmin × 6.5 arcmin field were determined using the IRAF *phot* task, utilizing the centroid centring algorithm on both images. The list of matched coordinates was then used as an input to the IRAF *geomap* task to derive a geometric transformation between the two images, allowing for translation, rotation and independent scaling in the x- and y-axes. The rms of the fit was 0.064 arcsec. Aperture photometry was then carried out on the WHT image for a host galaxy measurement and on the original PS1 image for a measurement of PS1-10ahf. The coordinates of the transient and of the host galaxy were measured in both images with three different centring algorithms provided by the *phot* task; centroid, Gaussian and optimal filtering. This provided a mean position and a standard deviation. The standard deviation of the three measurements was taken as the positional error measurement in x and y of the two objects. The x, y position of PS1-10ahf was then transformed to the coordinate system of the ACAM frame using the transformation defined by the 10 stars in common. A separation of 0.148 arcsec was determined (using a pixel scale for the ACAM instrument of 0.25 arcsec pixel^{-1})[8]. As before, the total uncertainty in the alignment of the two objects is hence the quadrature sum of the uncertainties in the centroids of the host and PS1-10ahf and the rms of the alignment transformation. This was found to be 0.214 arcsec at the pixel scale of ACAM, hence there is no evidence for an offset between the transient and the centroid of its host galaxy.

PS1-10ahf is coincident, within the errors, to the centroid of the host galaxy which does not offer the same strong argument of it not being QSO variability when compared with PS1-10pm being offset. However, the differences in the spectral features and the relatively low luminosity of PS1-10ahf compared to the Hall et al. (2002) QSO sample does not favour a QSO origin. Overall the comparisons above indicate a best match to a slowly evolving SLSN Ic of the same type as SN2007bi, PTF12dam and PS1-11ap (Gal-Yam et al. 2009; Young et al. 2010; Nicholl et al. 2013; McCrum et al. 2014).

[8] http://www.ing.iac.es/Astronomy/observing/instruments.html

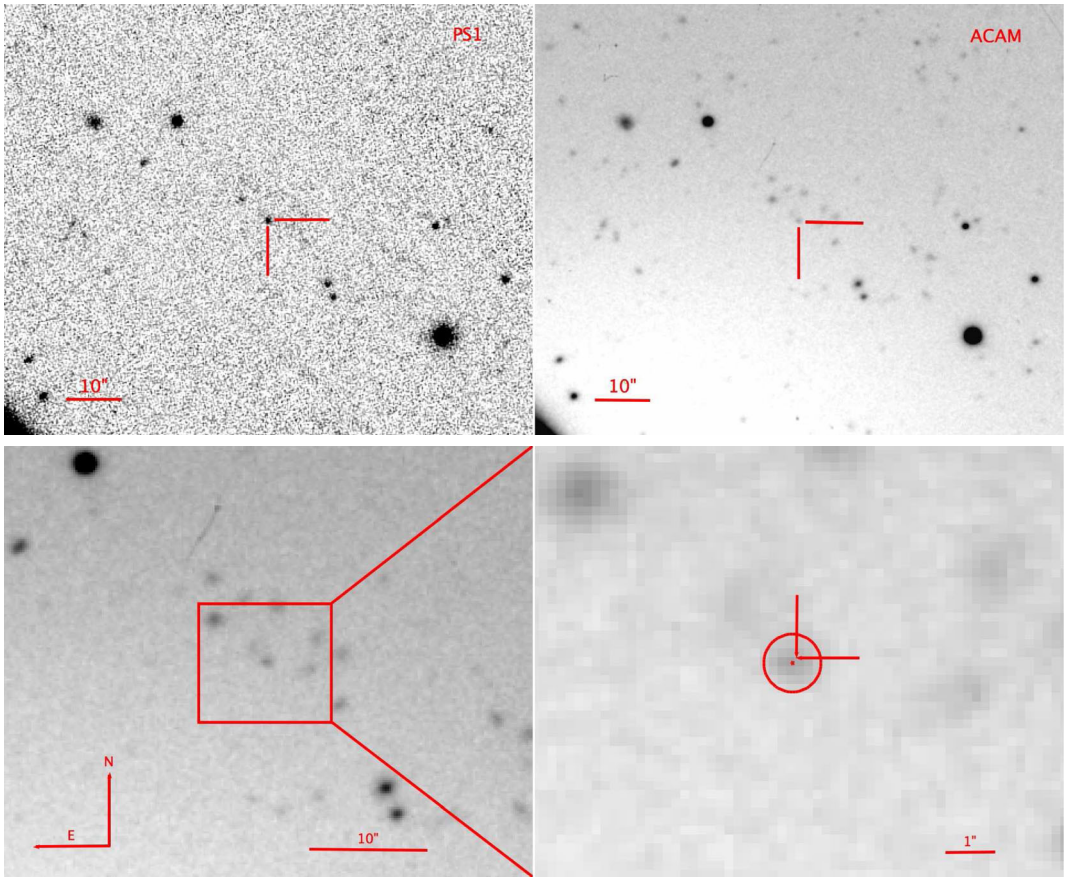

Figure 12. PS1 and WHT i_{P1}- and i-band images of the possible slowly evolving SLSN Ic PS1-10ahf at peak and after the explosion has faded. The circle in the zoomed, lower-right image is centred on the galaxy position with a radius corresponding to 3σ. The perpendicular lines in this image meet at the determined centroid of the transient position which is well within the determined central region of the galaxy. Although this does not rule out the object as a slowly evolving SLSN Ic, this result does not provide conclusive evidence that the transient is not an AGN-like event, unlike the poor spectral comparisons of PS1-10ahf with the Hall et al. (2002) QSOs.

5 DISCUSSION

5.1 SLSNe Ic in PS1

By a combination of two semi-automated transient alert pipelines and vigorous human screening, the catalogue of all the hostless transients from approximately the first year of the PS1 survey presented within can be considered to be comprehensive. Of the 12 spectroscopically confirmed, core-collapse PS1 SNe with faint host galaxies (see Table 5), 5 have been classified as SLSNe Ic independently of this paper; PS1-10ky and PS1-10awh (Chomiuk et al. 2011) and PS1-11ap (McCrum et al. 2014). PS1-11tt and PS1-11afv fall into the same category with high redshifts obtained from the identification of Mg II in their spectrum giving them comparable absolute magnitudes to the superluminous data set (Lunnan et al. 2014). Evidence from the spectrum and light curves of PS1-10pm provide convincing arguments that it is, in fact, another such event as shown in Section 4.1 of this paper. PS1-10ahf also seems to share characteristics with these objects, although possible reasons for classifying it as an AGN are given in Section 4.3. PS1-10afx was originally thought to be a superluminous event (Chornock et al. 2013) but more recently has been shown to be a lensed SN Ia (Quimby et al. 2013b, 2014). Despite this possible contamination, probing hostless transient objects with all SNe Ia removed appears to prove an efficient method of finding SLSNe Ic.

Fig. 13 uses literature data of published SLSNe Ic to illustrate the trend of SLSNe Ic having luminosities consistently brighter than their host galaxies and probes how this might evolve with redshift. We have used host galaxy and SLSNe Ic data from a range of sources for confirmed SLSNe Ic. The data are taken from this paper, Pastorello et al. (2010a), Quimby et al. (2011), Chomiuk et al. (2011), Berger et al. (2012), Chornock et al. (2013), Inserra et al. (2013), Lunnan et al. (2014), McCrum et al. (2014) and Nicholl et al. (2014). The peak apparent magnitudes of these SLSNe Ic are plotted along with the apparent magnitudes of their host galaxies, in the same observed filter.

We should highlight possible biases in interpreting this figure. At low redshift ($z < 0.5$) these SLSNe have been found in a range of surveys which searched for SNe in and outside bright galaxies, such as the PTF (Law et al. 2009) and La Silla QUEST (Baltay et al. 2013) However, both the CRTS (Drake et al. 2009) and the Pan-STARRS1 'Faint Galaxy Supernova Search' (Inserra et al. 2013) used catalogue matching which selected transients with significant flux differences between host object and transient. While there may be some bias in the CRTS and PS1 discovered objects no survey (or published study) has found an SLSN in a high mass, high luminosity host (with the threshold of roughly $M_g \sim -19$). Neither is there any explanation how this would arise in a survey selection bias. At redshifts above $z > 0.5$ (mostly PS1 objects in the MDS fields) the trend remains, but of course many of these objects have

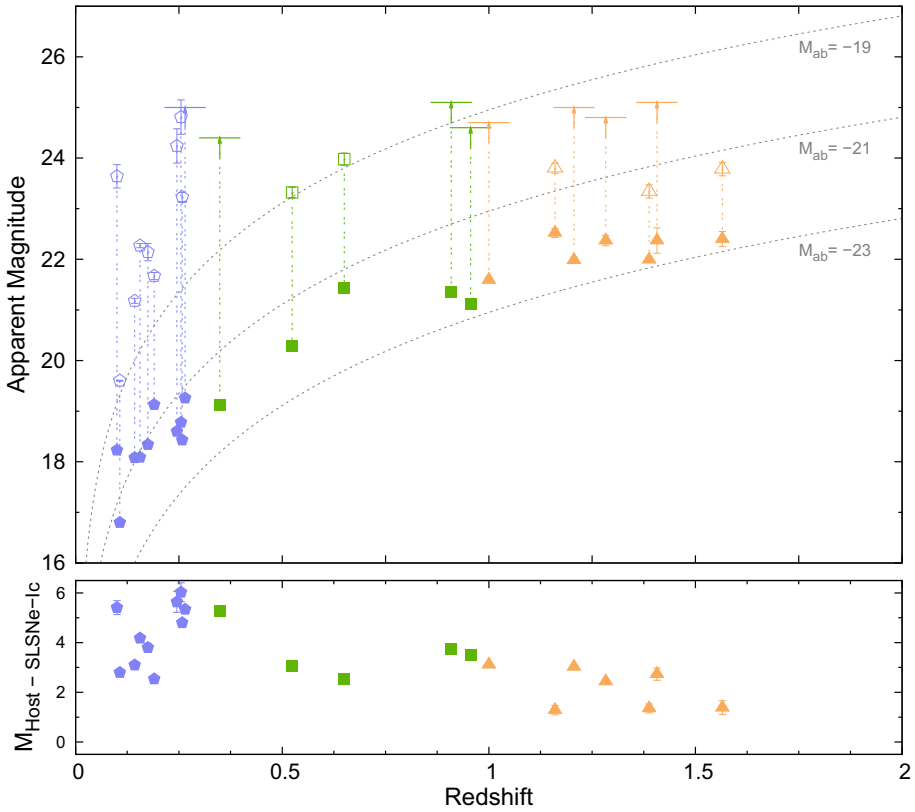

Figure 13. Observed SLSNe Ic apparent magnitudes (opaque shapes) compared with their host galaxy magnitudes (hollow shapes) in the same filter to emphasize the large differences between the two and thus support the method of finding SLSNe Ic given in the paper. The blue hexagons show V, g and g_{P1}-band data, the green squares show r and r_{P1}-band data and the yellow triangles show i and i_{P1}-band data. Any host galaxies with only limiting magnitudes are shown as arrows. Host galaxy data were taken from Lunnan et al. (2014) and Nicholl et al. (2014) and the SLSNe Ic data from various sources (see the text for more details). The three, grey dotted lines represent the trends given by constant absolute magnitudes of −23, −21 and −19 mag. The lower panel shows the magnitude difference between the SLSNe Ic and their hosts, plotted against the same redshift range as the upper plot.

been selected for classification in PS1 precisely because they have no obvious host galaxy as we have described in this paper. At redshifts below $z = 0.5$ the mean difference between host and peak SLSN Ic magnitude is at least 4.5 ± 1.2 mag. It appears to decrease to 2.2 ± 0.8 mag between redshifts 1 and 2 (note that the numbers quoted for the magnitude differences here include the limiting host galaxy magnitudes, meaning that they are lower limits on the magnitude difference).

Although there are caveats with the selection methods it is certainly true that no SLSN Ic below $z \sim 1.5$ has been found in a galaxy anywhere near the luminosity of a typical L^* galaxy. If normal and slowly evolving SLSNe Ic can occur in brighter galaxies at low redshift, the combined survey power of all professional and amateur searches have not uncovered any. Although this lack of evidence does not prove that these events cannot occur in such environments, the large number of SLSN Ic discoveries exclusively faint galaxies seems to suggest that such localities are preferential. Additionally, the plot suggests that there may be a trend for the host galaxies of SLSNe Ic to be systematically brighter at higher redshift. Although we have employed the technique of no visible host to select high-z candidates, this would not explain why the hosts look intrinsically *brighter* than at low redshift in this plot. We again emphasize that there may well be selection effects and further discoveries from low-z e.g. iPTF and LSQ + PESSTO (Nicholl et al. 2014) to high-z (e.g. the Dark Energy Survey) are required to shed further light on the host galaxies and expand on the detailed work of Lunnan et al. (2014).

Neill et al. (2011), Chen et al. (2013) and Lunnan et al. (2014) attribute the link between SLSN Ic and dwarf galaxies as being physically due to the low metallicities measured (where possible) for the hosts. If the mass–metallicity relation for galaxies evolves over redshift, one might expect a larger fraction of the massive galaxies (within a factor of 2 of $L^\star$) at redshifts beyond 1.5 to have significantly lower metallicity than their low-redshift counterparts. Erb et al. (2006) show that this is visible at $\langle z \rangle = 2.26 \pm 0.17$ with star-forming galaxies having metallicities which are typically 0.3 dex lower than low-z galaxies of similar mass. If there is a metallicity threshold beyond which SLSNe Ic are generally not formed due to progenitor evolution (Chen et al. 2013; Lunnan et al. 2014) then one night expect the mass–metallicity evolution of galaxies to cause SLSN Ic to appear in more massive, more luminous galaxies at higher redshift. We may be seeing this effect in the trend in Fig. 13, although the scatter is quite large and there are numerous non-detections at the higher redshifts. In addition, Cooke et al. (2012) present the discoveries of two transients with light curves that match SLSN Ic in galaxies with redshifts of $z = 2.05$ and 3.9. These transients were selected by virtue of being in galaxies with estimated photometric redshifts beyond $z > 2$ and the method has an obvious selection bias as their discovery required detection of a host galaxy. However, the difference between host galaxy and

transient magnitudes are only +0.3 and −0.18 mag. This would suggest the trend in Fig. 13 could continue up to higher redshift, but this requires further work in selecting SLSN at redshifts beyond $z = 2$.

Of interest is the lack of SLSNe II discoveries within this data set. This could suggest an intrinsically lower rate for this particular brand of SLSNe or it could be evidence of the observational bias apparent in this investigation. The small number of SLSNe II discovered so far have been associated with brighter hosts, which could explain the lack of discoveries here. It is noted here for completeness that some SLSNe II have been found in dwarf galaxies (e.g. SN2006tf; Smith et al. 2008; Neill et al. 2011).

5.2 Monte Carlo simulations and estimate of SLSNe Ic rates

Previous works have carried out rough estimates of the rates of SLSN Ic to provide an initial guide to the relative frequency of these transients compared to the normal SN population. Quimby et al. (2011) estimated their relative rate to be around 1 in every 10 000 CCSN. From the detection of just one event in the Texas Supernova Search (SN2005ap), Quimby et al. (2013a) estimated the SLSN Ic rate to be 32^{+77}_{-26} events Gpc^{-1} yr^{-1} h^3_{71}. An estimation of the rate with respect to the CCSN rate (within the same volume) is a useful parameter as it can constrain theories of the progenitor sources, as has been done with GRB and broad-lined SNe Ic (or hypernova; e.g. Podsiadlowski et al. 2004). It appears that long duration GRBs rates (LGRBs) are around 1 in every 1000 CCSNe (Ghirlanda et al. 2013) hence the initial rates in Quimby et al. (2011) would suggest a very low volumetric rate, roughly 10 times rarer than LGRBs. Quimby et al. (2013a) also compared their volumetric rate to the CCSN rate in Botticella et al. (2008), to estimate a relative rate of SLSN Ic to CCSN of 1 in 1000–20 000. In many of these, the rate of the rare transients (GRBs or SLSN) with respect to the CCSN population is assumed to be relatively constant with redshift. This is certainly an unknown factor and may evolve due to the metallicity of the bulk of the star formation changing. Since we have low numbers of objects we will assume here that the ratio is constant.

Young et al. (2008) used Monte Carlo simulations to estimate the number of CCSNe expected to be discovered in all sky transient surveys such as PS1. Since the publication of this paper, the study of SLSNe has rapidly evolved (for a recent review see Gal-Yam 2012). We use the same Monte Carlo code from Young et al. (2008) (recoded in PYTHON) and have updated the input data to include light curves and spectra from SLSNe Ic and their slowly evolving, SN2007bi-like counterparts. This allows a calculation of the rates of these SLSNe Ic from the detections in the PS1 MDS orphan population. We can determine a robust lower limit and a reasonable estimate of the most likely range for the rates within a redshift of approximately $z < 1.4$.

The simulations were tailored specifically for the PS1 MDS; taking into account observational cadence, limiting magnitudes and historical records of time lost due to bad weather, technical difficulties or scheduled maintenance. A foreground extinction of $E(B - V) = 0.023$ is assumed which is typical for the Galactic line of sight for the MDS fields. No internal galaxy extinction is applied, which is a reasonable assumption for the SLSNe Ic found to date. The simulations run in two stages. The first stage simulates 10 000 SN events with a population demographic mimicking the input SNe light curves, spectral data bases, CCSN to star formation ratio and star formation history, all within a volume between $0.3 < z < 1.4$. The second stage determines the fraction of these events the PS1 survey would have discovered.

To estimate the limiting magnitude of the MDS images and the efficiency of recovering transients we ran multiple fake star tests. Five nightly stacks of skycell #39 (which is approximately one of the 60 CCDs in the focal plane array, warped to the sky) in MD08 were taken from September 2010, with FWHM of point sources between 1.2 and 1.6 arcsec. Fake stars were added at magnitudes of 21, 22, 23, 24 and 25 (including shot noise) at approximately 80 separate positions on the skycell. When simulating sources of >21 mag only sparse detection efficiency curves are produced and so the points were fitted with an 'S-function' (see equation 1 in Dahlen, Strolger & Riess 2008). This allowed precise determination of the detection efficiencies. Half of these were on empty sky regions, to simulate the orphan population and the other half were placed inside resolved galaxies. The IPP image subtraction routine (*ppSub*) was run using a reference image made of a stack which contained 86 individual images. This is a typical static reference sky product that was used during the period of searching of these transients, and had an image quality of 1.1 arcsec. Sources were catalogued in the difference image, and clear visual detections (in a similar way to how the manual screening was done in the real transient search) were picked for photometric measurements with PSF fitting, as described in Section 2. The detection efficiency fell below 98 per cent at the following r_{P1}-band magnitudes: 22.8 (in seeing of 1.6 arcsec), 22.9 (1.4 arcsec), 23.3 (1.2 arcsec), 23.6 (1.0 arcsec). Hence, we take the r_{P1}-band limiting magnitude to be 23 as the median seeing of individual PS1 images are in the range 1.3 to 1.1 arcsec (g_{P1} through z_{P1}). We assume similar for g_{P1} and i_{P1} bands as the exposure times for these are set to retrieve the same limiting magnitude and previous estimates of depth have found the same (e.g. see the extensive discussion in Tonry et al. 2012a). For the z_{P1} band we conservatively take the depth to be 22.4.

For each of the 10 000 SNe simulated, the simulations use rest-frame SNe spectra to calculate the *K*-corrections attributed to the SN at its assigned redshift for each of the PS1 $griz_{P1}$ filters. To this end, the simulations require a complete spectral series, covering both the full wavelength and temporal ranges required to generate all possible *K*-corrections, for each of the two SLSNe Ic classes. As no single object data set fulfilled these specifications, composite spectral series were made for the normal and slowly evolving SLSNe Ic classes. The slowly evolving SLSNe Ic series uses data from PTF12dam and PS1-11ap (Nicholl et al. 2013; McCrum et al. 2014) and the SLSNe Ic series uses SN2010gx, PTF09cnd, PS1-10ky, SN2011ke, SN2012il and PS1-10pm data (Pastorello et al. 2010a; Chomiuk et al. 2011; Quimby et al. 2011; Inserra et al. 2013; this paper). Even with data from all the aforementioned SLSNe Ic however, the full wavelength coverage required for the Young et al. (2008) simulations to work was still not reached at all epochs, particularly at late times when the SLSNe Ic had become much fainter than their peak magnitudes. To extend the spectra bluewards, blackbody fits were employed to extrapolate the observed data. The 38, 65 and 185 d slowly evolving SLSNe Ic epochs were fitted with 8500, 7500 and 6500 K blackbody SEDs, respectively. 16 000, 7000 and 6500 K blackbody SEDs best fitted the −21, 50 and 115 d SLSNe Ic epochs. The complete spectral series used for both of these SLSNe Ic classes can be seen in Fig. A2.

As each spectrum consists of data from multiple sources, the flux of each epoch had to be scaled to accurately represent the class in question. A PS1-11ap absolute magnitude g_{P1}-band light curve was used as a template for the slowly evolving class and absolute *r*-band SN2011ke data was used for the SLSNe Ic class. We set the absolute

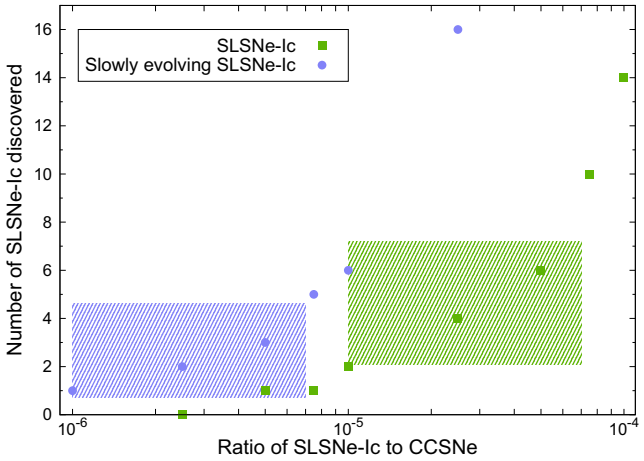

Figure 14. The results of the Monte Carlo simulations. The two shaded boxes represent the number of probable SLSNe Ic (green) and slowly evolving SLSNe Ic (blue) discovered during the search for orphans presented within the paper. The points represent the ratios of SLSNe Ic to CCSNe against the number of SLSNe Ic discovered within the simulation during the same time period. Thus, we can deduce the approximate rate of SLSNe Ic, of both the normal and the more rare, slowly evolving types.

peak magnitude distributions to be $M_{\rm AB} = -21.5 \pm 0.3$ for the normal SLSNe Ic and $M_{\rm AB} = -21.25 \pm 0.5$ for the slowly evolving SLSNe Ic, based on the observed spread of absolute magnitudes that can be seen in Figs 5 and 10 of this paper and in published literature such as Inserra et al. (2013), McCrum et al. (2014) and Inserra & Smartt (2014), the latter of which provide the largest compilation of absolute magnitudes of SLSNe to date. To scale each spectrum, the *calcphot* task of the SYNPHOT[9] package within IRAF was utilized to deduce synthetic absolute magnitude values using an appropriate filter. Each spectrum was simply multiplied by a constant until the synthetic magnitude matched that of the template light curve at the same phase. The SDSS filters built-in to *calcphot* were used for this rough comparison but the closeness of their filter functions to that of the PS1 filters of the template light curves is more than adequate.

For a simulated SN event to be classified as 'discovered', we required that the object peaked above an AB magnitude of 22 (in any band), and had a light curve which was detectable above the limiting magnitudes listed above for 100 d in the observer frame (in at least one band). In the PS1 survey we spectroscopically detected 7 SLSNe Ic as listed in Table 5. PS1-10awh was detected for 75 d above the set detection limits and did not strictly meet the criteria. Hence we will consider that we have six SLSNe Ic detected (and also check this with a separate Monte Carlo calculation with the criterion for detection set at 75 d). While this is almost certainly incomplete it serves as a baseline observational comparison for the simulated rates and allows lower limits to be placed on the volumetric rates and plausible ranges to be discussed.

We consider the slowly evolving, SLSNe Ic and the SLSNe Ic separately. Fig. 14 uses this information to illustrate the range of possible SLSNe Ic/CCSNe ratios by comparing the observed data with the results of the Monte Carlo simulations carried out here. For the simulation to mimic the four standard SLSNe Ic which were spectroscopically found during the hostless transient search presented (Table 5), the ratio of SLSNe Ic to CCSNe has to be set to $3^{+3}_{-2} \times 10^{-5}$ in the Monte Carlo simulation (with error values corresponding to 1σ Gaussian limits taken from Gehrels 1986, rounded to one decimal place). The slowly evolving type, of which only two possible events were discovered during the first year of the PS1 MDS, are likely less common and their simulated rate was determined to be only $3^{+4}_{-2} \times 10^{-6}$ of the CCSNe rate. As the slowly evolving SLSNe Ic remain brighter for a longer duration after their peak luminosity, they should be easier to detect and hence the fact that we have spectroscopically confirmed fewer of these than the faster declining SLSNe Ic suggests that they are indeed rarer. This is in agreement with previous suggestions of Gal-Yam (2012) and Nicholl et al. (2013). As a comparison, we ran the Monte Carlo calculation with the requirement of 75 d, and hence included PS1-10awh as a detected event. We found a relative rate of $\sim 10^{-5}$, within the error bar of our estimated result of $3^{+3}_{-2} \times 10^{-5}$.

However, we cannot be confident that we are spectroscopically complete and there could well be SLSNe Ic in Tables 6 and A2 which have not been spectroscopically confirmed. There are 10 possible SNe in these tables which peak above $M_{\rm AB} = 22$ and do not have a confident Type Ia light-curve classification. If we regard these as potential SLSNe Ic which we have not managed to classify then the ratio of normal CCSNe to SLSNe Ic in our spectroscopically confirmed sample would suggest that approximately 60 per cent of them could be SLSNe Ic. Thus, we consider a plausible upper limit to the number of SLSNe Ic in our total detected PS1 MDS sample to be 10^{+4}_{-3} (with errors again estimated from Gehrels 1986), which would imply an upper limit to the rate of $8^{+2}_{-1} \times 10^{-5}$ SLSNe Ic per CCSNe.

In summary, we have estimated a range for the rate of SLSNe Ic compared to the rate of CCSNe within a redshift of $0.3 \leq z \leq 1.4$ of between $3^{+3}_{-2} \times 10^{-5}$ and $8^{+2}_{-1} \times 10^{-5}$. The rate of the slowly evolving, SN2007bi-like SLSNe Ic appear to be a factor of $\sim$10 lower and likely to be around 3×10^{-6}, although this number is uncertain by about a factor of 2 given the small numbers detected. To put this in context and compare with the only other quantitative rate calculation (albeit at lower redshift), we find there is about one SLSN Ic per 12 000–30 000 CCSNe; whereas Quimby et al. (2013a) find one per 1000–20 000. This compares to the rate of LGRBs of around 1 in every 1000 CCSNe (Ghirlanda et al. 2013).

6 CONCLUSIONS

We have catalogued all the SN-like, hostless transients from the PS1 MDS and, by using multiple spectroscopic programmes and photometric classifiers, filtered out all the SNe Ia events. This leaves a promising percentage of remaining objects that seem to fall into the category of SLSNe Ic.

(i) 249 hostless transients were discovered within the first 1.37 yr of the PS1 MDS, 133 of which have SN-like features.

(ii) 40 are spectroscopically confirmed SNe, $\sim$17.5 per cent of which are possible SLSNe Ic.

(iii) 12 are spectroscopically confirmed, non-SNe Ia, $\sim$60 per cent of which are possible SLSNe Ic.

PS1-10pm and PS1-10ahf were discovered in this way. Photometric and spectroscopic comparisons place PS1-10pm comfortably in the SLSNe Ic class. The classification of PS1-10ahf is not as robust, but reasonably solid photometric and spectroscopic comparisons give it a probable association with the slowly evolving class of SLSNe Ic such as SN2007bi, PS1-11ap and PTF12dam. We highlight that this was a combination of spectroscopic classification (when the SNe were close to peak) and photometric classification

[9] http://www.stsci.edu/institute/software_hardware/stsdas/synphot

after the light curves had been gathered. A challenge remains to carry out accurate photometric classification in real time.

Using the SLSNe Ic statistics gathered during the search for orphans and comparing them with Monte Carlo simulations of SLSNe Ic, we determined the rate of SLSNe Ic within a redshift of $0.3 \leq z \leq 1.4$ to be between $3^{+3}_{-2} \times 10^{-5}$ and $8^{+2}_{-1} \times 10^{-5}$ that of the CCSNe rate. The ratio of slowly evolving SLSNe Ic to CCSNe seems to be much lower, at around $3^{+4}_{-2} \times 10^{-6}$.

Using a combination of careful photometric analysis and thorough spectroscopic follow-up and the search method of exploiting the common characteristic of the >2 mag difference between discovered SLSNe Ic peak magnitudes and their host galaxies, an ever increasing number of SLSNe Ic should be found in the next few years from current and future wide-field surveys (Pan-STARRS2, The Dark Energy Survey, The Zwicky Transient Factory, La Silla-QUEST + the Public ESO Spectroscopic Survey of Transient Objects and Large Synoptic Survey Telescope).

ACKNOWLEDGEMENTS

The Pan-STARRS1 Surveys (PS1) have been made possible through contributions of the Institute for Astronomy, the University of Hawaii, the Pan- STARRS Project Office, the Max-Planck Society and its participating institutes, the Max Planck Institute for Astronomy, Heidelberg and the Max Planck Institute for Extraterrestrial Physics, Garching, The Johns Hopkins University, Durham University, the University of Edinburgh, Queen's University Belfast, the Harvard–Smithsonian Center for Astrophysics, the Las Cumbres Observatory Global Telescope Network Incorporated, the National Central University of Taiwan, the Space Telescope Science Institute, the National Aeronautics and Space Administration under grant no. NNX08AR22G issued through the Planetary Science Division of the NASA Science Mission Directorate, the National Science Foundation under grant no. AST-1238877, and the University of Maryland. SJS acknowledges funding from the European Research Council under the European Union's Seventh Framework Programme (FP7/2007-2013)/ERC Grant agreement no. [291222] (PI: SJS). This work is based on observations made with the following telescopes: William Herschel Telescope (operated by the Isaac Netwon Group), in the Spanish Observatorio del Roque de los Muchachos of the Instituto de Astrofisica de Canarias, in the island of La Palma; the Gemini Observatory, which is operated by the Association of Universities for Research in Astronomy, Inc., under a cooperative agreement with the NSF on behalf of the Gemini partnership: the National Science Foundation (USA), the National Research Council (Canada), CONICYT (Chile), the Australian Research Council (Australia), Ministério da Ciência, Tecnologia e Inovação (Brazil) and Ministerio de Ciencia, Tecnología e Innovación Productiva (Argentina). Some observations reported here were obtained at the MMT Observatory, a joint facility of the Smithsonian Institution and the University of Arizona. Support for SAR was provided by NASA through Hubble Fellowship grant #HST-HF-51312.01 awarded by the Space Telescope Science Institute, which is operated by the Association of Universities for Research in Astronomy, Inc., for NASA, under contract NAS 5-26555. JLT acknowledges support for this work provided by National Science Foundation grant AST-1009749. SM acknowledges financial support from the Academy of Finland (project: 8120503). We thank A. Gal-Yam and P. Nugent for providing the classification of PS1-11acn, which is the PTF object PTF11dws.

Facilities: Pan-STARRS1, Gemini, William Herschel Telescope.

REFERENCES

Abazajian K. N. et al., 2009, ApJS, 182, 543
Adami C. et al., 2006, A&A, 451, 1159
Arcavi I. et al., 2010, ApJS, 721, 777
Arnett W. D., 1982, ApJ, 253, 785
Baltay C. et al., 2013, PASP, 125, 683
Barbary K. et al., 2009, ApJ, 690, 1358
Barkat Z., Rakavy G., Sack N., 1967, Phys. Rev. Lett., 18, 379
Berger E. et al., 2012, ApJ, 755, L29
Bond J. R., Arnett W. D., Carr B. J., 1984, ApJ, 280, 825
Botticella M. T. et al., 2008, A&A, 479, 49
Cardelli J. A., Clayton G. C., Mathis J. S., 1989, ApJ, 345, 245
Chen T.-W. et al., 2013, ApJ, 763, L28
Chevalier R. A., Irwin C. M., 2011, ApJ, 729, L6
Chomiuk L. et al., 2011, ApJ, 743, 114
Chornock R. et al., 2013, ApJ, 767, 162
Cooke J. et al., 2012, Nature, 491, 228
Dahlen T., Strolger L.-G., Riess A. G., 2008, ApJ, 681, 462
Drake A. J. et al., 2009, ApJ, 696, 870
Draper P. W., Berry D. S., Jenness T., Economou F., 2009, ASP Conf. Ser. Vol. 411, Astronomical Data Analysis Software and Systems XVIII. Astron. Soc. Pac., San Francisco, p. 575
Erb D. K., Shapley A. E., Pettini M., Steidel C. C., Reddy N. A., Adelberger K. L., 2006, ApJ, 644, 813
Foltz C. B., Wilkes B., Weymann R., Turnshek D., 1983, PASP, 95, 341
Fowler W. A., Hoyle F., 1964, ApJS, 9, 201
Gal-Yam A., 2012, Science, 337, 927
Gal-Yam A. et al., 2009, Nature, 462, 624
Gal-Yam A. et al., 2011, Astron. Telegram, 3403, 1
Gehrels N., 1986, ApJ, 303, 336
Gezari S. et al., 2012, Nature, 485, 217
Ghirlanda G. et al., 2013, MNRAS, 428, 1410
Hall P. B. et al., 2002, ApJS, 141, 267
Heger A., Woosley S. E., 2002, ApJ, 567, 532
Hogg D. W., Baldry I. K., Blanton M. R., Eisenstein D. J., 2002, preprint (astro-ph/0210394)
Howell D. A. et al., 2013, ApJ, 779, 98
Inserra C., Smartt S. J., 2014, ApJ, 796, 87
Inserra C. et al., 2013, ApJ, 770, 128
Kaiser N. et al., 2010, Proc. SPIE, 7733, 12K
Kasen D., Bildsten L., 2010, ApJ, 717, 245
Law N. M. et al., 2009, PASP, 121, 1395
Leaman J., Li W., Chornock R., Filippenko A. V., 2011, MNRAS, 412, 1419
Leloudas G. et al., 2012, A&A, 541, A129
Lunnan R. et al., 2013, ApJ, 771, 97
Lunnan R. et al., 2014, ApJ, 787, 138
McCrum M. et al., 2014, MNRAS, 437, 656
Magnier E., 2006, in Ryan S., ed., Proc. AMOS Conf. Vol. 2, The Pan-STARRS PS1 Image Processing Pipeline. The Maui Economic Development Board, Maui, HI, p. 455
Magnier E., 2007, ASP Conf. Ser. Vol. 364, The Future of Photometric, Spectrophotometric and Polarimetric Standardization. Astron. Soc. Pac., San Francisco, p. 153
Magnier E. A., Liu M., Monet D. G., Chambers K. C., 2008, Proc. IAU Symp. 248, A Giant Step: From Milli- to Micro-Arcsecond Astrometry. Cambridge Univ. Press, Cambridge, p. 553
Neill J. D. et al., 2011, ApJ, 727, 15
Nicholl M. et al., 2013, Nature, 502, 346
Nicholl M. et al., 2014, MNRAS, 444, 2096
Ofek G. O., 2007, ApJ, 659, L13
Ostriker J. P., Gunn J. E., 1971, ApJ, 164, L95
Pastorello A. et al., 2010a, ApJ, 724, L16
Pastorello A. et al., 2010b, Astron. Telegram, 2504, 1
Perets H. B. et al., 2010, Nature, 465, 322
Podsiadlowski P., Mazzali P. A., Nomoto K., Lazzati D., Cappellaro E., 2004, ApJ, 607, L1
Quimby R. M. et al., 2011, Nature, 474, 487

Quimby R. M., Yuan F., Akerlof C., Wheeler J. C., 2013a, MNRAS, 431, 912
Quimby R. M. et al., 2013b, ApJ, 768, L20
Quimby R. M. et al., 2014, Science, 344, 396
Rest A. et al., 2005, ApJ, 634, 1103
Rest A. et al., 2011, ApJ, 729, 88
Rest A. et al., 2014, ApJ, 795, 44
Rodney S. A., Tonry J. L., 2009, ApJ, 707, 1064
Rodney S. A., Tonry J. L., 2010, ApJ, 715, 323
Sako M. et al., 2008, ApJ, 135, 348
Sako M. et al., 2011, ApJ, 738, 162
Schechter P., 1976, ApJ, 203, 297
Schlegel D. J., Finkbeiner D. P., Davis M., 1998, ApJ, 500, 525
Scolnic D. et al., 2014, ApJ, 795, 45
Smartt S. J., Maund J. R., Hendry M. A., Tout C. A., Gilmore G. F., Mattila S., Benn C. R., 2004, Science, 303, 499
Smith N. et al., 2007, ApJ, 666, 1116
Smith N., Chornock R., Li W., Ganeshalingam M., Silverman J. M., Foley R. J., Filippenko A. V., Barth A. J., 2008, ApJ, 686, 467
Stubbs C. W., Doherty P., Cramer C., Narayan G., Brown Y. J., Lykke K. R., Woodward J. T., Tonry J. L., 2010, ApJS, 191, 376
Sullivan M. et al., 2006, ApJ, 648, 868
Thompson T. A., Chang P., Quataert E., 2004, ApJ, 611, 380
Tonry J. L. et al., 2012a, ApJ, 745, 42
Tonry J. L. et al., 2012b, ApJ, 750, 99
Valenti S. et al., 2010, Cent. Bur. Electron. Telegrams, 2214, 1
Young D. R., Smartt S. J., Mattila S., Tanvir N. R., Bersier D., Chambers K. C., Kaiser N., Tonry J. L., 2008, A&A, 489, 359
Young D. R. et al., 2010, A&A, 512, A70

APPENDIX A: OBJECT TABLES AND EXAMPLE PS1 PHOTOMETRY

Table A1. *Subaru* host detections for some of the orphans presented within the paper and their z-band magnitudes. The last four objects had no associated host and so only a limiting magnitude, again in the z band, is available.

PS1 ID	M_z (dz)	PS1 ID	M_z (dz)
PS1-10ahq	22.818 (0.053)	PS1-10abf	>24.933
PS1-10aht	23.864 (0.201)	PS1-10awh	>24.625
PS1-10afx	22.512 (0.075)	PS1-10ky	>25.049
PS1-10dq	25.380 (0.470)	PS1-11er	>23.510
PS1-11ad	23.626 (0.248)		

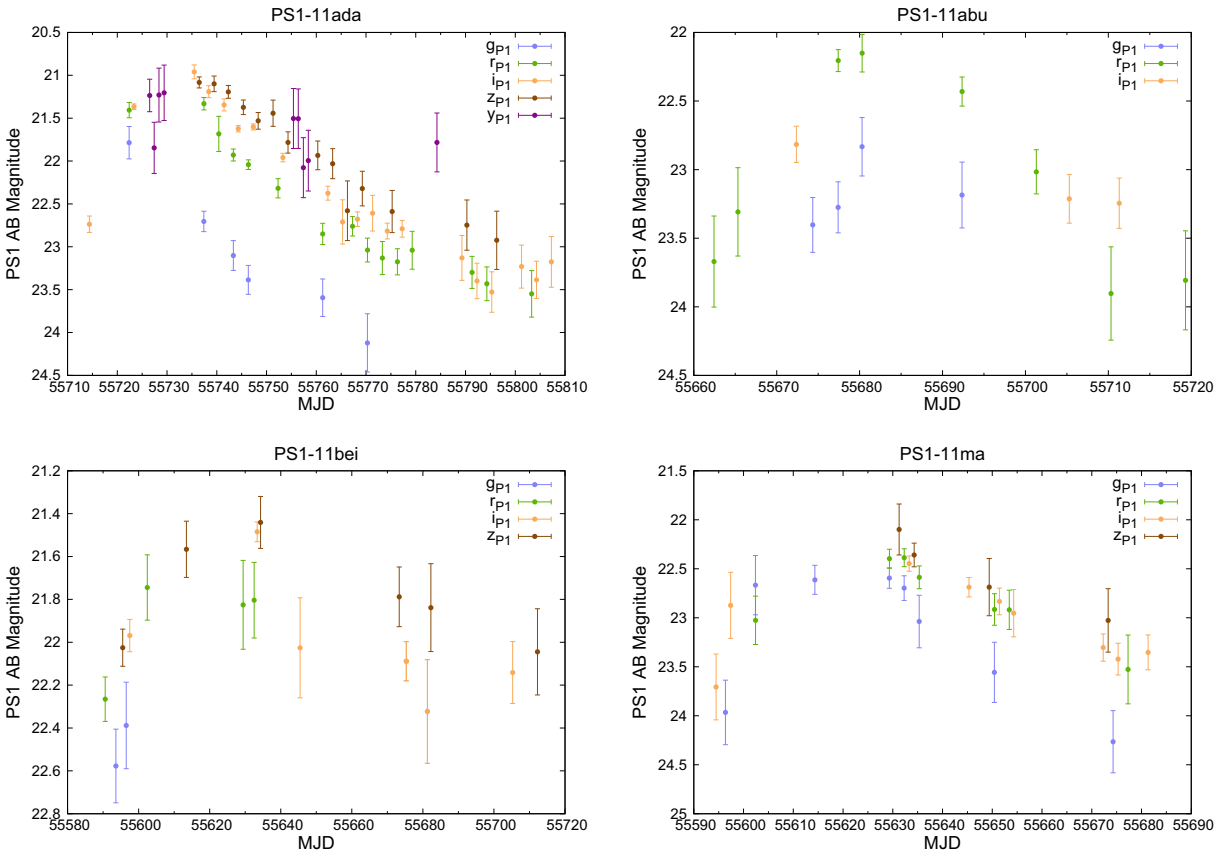

Figure A1. Example light curves from a selection of orphans from Table A2. These transients were hand picked for having typical SN-like light curves exemplified by single, asymmetric peaks.

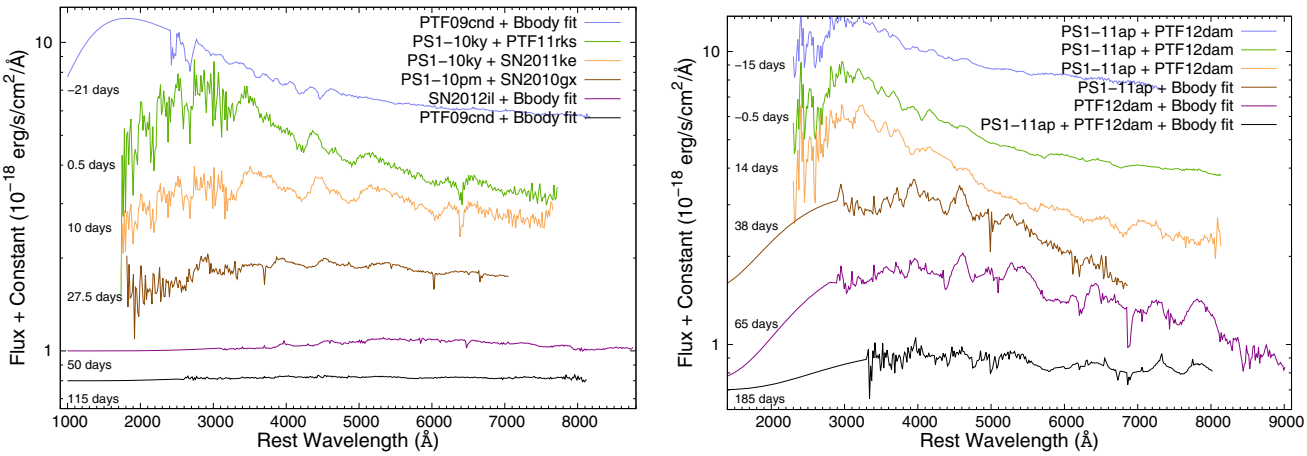

Figure A2. The composite spectral series' for the normal (left-hand figure) and slowly evolving (right-hand figure) SLSNe Ic classes. Each spectrum is composed of a mix of objects of the same class at similar epochs and appropriate blackbody curves, as indicated in the figure keys.

Table A2. 28 SN-like orphans. The numbers in the SOFT and PSNID columns represent the probability that the algorithms classified an object as the SN types given in brackets. Although none of these objects met with the confidence restrictions placed upon the photometric classifiers for identifying SNe (see Tables 4 and 6 for objects that do), it can be seen here that a large number of these objects were given some sort of tentative, photometric SNe classification.

Field	PS1 ID	RA (deg, J2000)	Dec. (deg, J2000)	SOFT	PSNID	Peak r_{P1}
MD01	PS1-10bku	35.5355	−5.1926	0.721 (Ia)	0.937 (Ia)	22.389 (0.089)
MD01	PS1-10ags	34.8215	−4.0770	1 (Ibc)	1 (II)	21.894 (0.076)
MD02	PS1-10bkj	54.0300	−27.6676	0.964 (Ia)	0.84 (Ibc)	21.773 (0.084)
MD03	PS1-10bkc	130.4508	43.2094	1 (IIL)	0.999 (Ibc)	21.968 (0.081)
MD03	PS1-10bmj	130.7928	43.9931	0.777 (Ia)	0.995 (Ibc)	22.640 (0.186)
MD03	PS1-10bll	131.2202	42.9031	0.616 (Ia)	0.939 (Ibc)	22.580 (0.120)
MD04	PS1-11ac	149.6572	1.3447	0.73 (Ia)	–	22.992 (0.163)
MD04	PS1-11cq	149.7889	1.6694	0.63 (Ia)	0.536 (Ibc)	22.902 (0.161)
MD04	PS1-11ma	150.7541	2.9919	–	0.976 (Ia)	22.387 (0.091)
MD04	PS1-11vp	150.8929	1.1808	–	–	22.453 (0.177)
MD04	PS1-11ax	151.0974	2.6413	0.512 (Ia)	0.924 (Ibc)	22.657 (0.140)
MD05	PS1-11bei	159.8550	59.2007	–	–	21.740 (0.150)
MD05	PS1-10vj	159.6722	58.8748	0.759 (Ia)	0.953 (Ia)	22.255 (0.110)
MD06	PS1-11jl	183.4510	48.0142	0.493 (Ia)	0.994 (Ibc)	22.702 (0.134)
MD06	PS1-10tk	185.4339	46.2052	0.996 (Ibc)	0.984 (Ia)	22.468 (0.162)
MD06	PS1-11zh	185.7641	46.2110	–	–	22.407 (0.080)
MD06	PS1-11abu	183.0532	47.7119	–	–	22.151 (0.137)
MD06	PS1-11yd	184.9034	46.0195	–	–	22.234 (0.088)
MD06	PS1-11za	183.6234	47.8537	–	–	21.924 (0.055)
MD06	PS1-11xq	184.2742	46.0311	–	–	22.367 (0.105)
MD07	PS1-11pe	212.0687	53.4873	–	0.784 (Ia)	21.916 (0.092)
MD07	PS1-11vq	213.6972	52.3841	–	–	22.508 (0.184)
MD08	PS1-10mc	244.9956	54.4228	0.527 (Ibc)	1 (Ia)	22.374 (0.120)
MD08	PS1-11agk	242.0433	55.4815	–	–	23.021 (0.335)
MD08	PS1-11ada	243.8752	53.8923	–	–	21.186 (0.100)
MD09	PS1-10byu	333.6330	1.1939	0.585 (Ia)	0.62 (Ia)	21.923 (0.145)
MD10	PS1-10ceu	351.6930	0.3734	–	–	21.480 (0.030)
MD10	PS1-10bkh	352.5808	−0.4692	0.748 (Ia)	0.941 (Ia)	23.126 (0.195)

Table A3. The 116 unknown orphans. The acronyms in the 'LC Status' column refer to the reasons why an attempt at classification has not been made. 'INC' objects have incomplete light curves, 'VAR' objects have variable light curves with no obvious trend and 'FAINT' objects fall out of the magnitude range for spectroscopic or reliable photometric classification. Objects with 'RED' status had no detections in the g_{P1}- or r_{P1}-band filters but showed a faint peak in the i_{P1}- and z_{P1}-band filters, possibly as a result of a single, energetic outburst such as an SN at high redshift.

Field	PS1 ID	RA (deg, J2000)	Dec. (deg, J2000)	Peak r_{P1}	LC Status	Field	PS1 ID	RA (deg, J2000)	Dec. (deg, J2000)	Peak r_{P1}	LC Status
MD01	PS1-10zw	35.0206	−4.0609	22.813 (0.151)	INC	MD05	PS1-11aaq	161.1660	59.4033	21.885 (0.073)	INC
MD01	PS1-10zt	35.9310	−4.1083	22.573 (0.111)	INC	MD06	PS1-10sr	186.7873	46.7462	22.320 (0.143)	INC
MD01	PS1-10adm	36.0926	−5.6325	23.096 (0.274)	VAR	MD06	PS1-10sl	185.5830	45.9826	22.513 (0.118)	INC
MD01	PS1-11db	37.0777	−4.2684	21.560 (0.087)	INC	MD06	PS1-10yq	183.4461	47.1259	22.776 (0.133)	FAINT
MD01	PS1-11eu	35.2756	−3.1914	23.445 (0.244)	FAINT	MD06	PS1-10xs	185.2658	46.5539	22.884 (0.140)	INC
MD01	PS1-10cal	35.5671	−4.5893	23.711 (0.326)	FAINT	MD06	PS1-10yl	185.9299	46.2831	22.462 (0.133)	FAINT
MD01	PS1-10ceo	35.0395	−5.0884	23.010 (0.110)	VAR	MD06	PS1-10ys	184.5287	47.7259	22.600 (0.149)	FAINT
MD01	PS1-10cep	35.1032	−3.5826	23.010 (0.110)	FAINT	MD06	PS1-10xt	184.2873	46.1409	23.265 (0.164)	INC
MD01	PS1-10bkt	36.0372	−2.7882	21.505 (0.066)	–	MD06	PS1-10jm	184.4595	47.4467	21.104 (0.097)	–
MD02	PS1-10agq	52.8398	−28.5254	23.008 (0.184)	VAR	MD06	PS1-10cef	185.2454	46.0920	23.150 (0.210)	FAINT
MD02	PS1-10ces	54.4704	−28.1703	22.780 (0.130)	VAR	MD06	PS1-11bet	184.4993	46.1507	22.530 (0.220)	FAINT
MD02	PS1-11beh	52.0673	−27.8645	22.780 (0.150)	INC	MD06	PS1-11jq	186.0334	47.9493	22.347 (0.080)	INC
MD02	PS1-11bej	52.5304	−29.0150	23.150 (0.230)	INC	MD06	PS1-11jt	186.3847	48.1535	22.457 (0.120)	INC
MD02	PS1-10aff	52.8698	−27.0436	–	RED	MD06	PS1-11qc	184.7770	47.6353	23.258 (0.279)	FAINT
MD02	PS1-10cer	53.9535	−28.9196	22.440 (0.090)	FAINT	MD06	PS1-11wm	183.6975	48.1353	22.586 (0.228)	FAINT
MD02	PS1-11bes	54.2109	−27.2108	23.260 (0.150)	INC	MD06	PS1-11vh	185.6786	47.0719	22.389 (0.105)	FAINT
MD02	PS1-10ceq	54.3060	−28.5226	–	RED	MD07	PS1-10vm	213.3563	52.3595	21.891 (0.109)	VAR
MD03	PS1-10cet	131.8517	44.6298	23.450 (0.200)	VAR	MD07	PS1-11fr	212.3379	53.6687	22.347 (0.282)	INC
MD03	PS1-11bem	130.0729	44.9492	23.360 (0.230)	INC	MD07	PS1-11fo	211.3801	53.4676	22.821 (0.347)	INC
MD03	PS1-10awt	132.1807	44.8813	22.125 (0.076)	VAR	MD07	PS1-11ahj	213.8155	54.3847	22.690 (0.150)	VAR
MD03	PS1-10cat	129.0721	45.1472	22.915 (0.157)	VAR	MD07	PS1-10ceg	213.4535	52.7237	23.090 (0.200)	INC
MD03	PS1-10ayj	129.5958	44.7852	–	RED	MD07	PS1-10ceh	214.5734	54.1141	22.800 (0.190)	FAINT
MD03	PS1-10can	129.8584	43.7600	22.677 (0.217)	VAR	MD07	PS1-11bel	214.3710	52.3339	–	INC
MD03	PS1-10cae	129.1859	44.5547	22.584 (0.101)	–	MD07	PS1-10jn	212.3330	54.2624	22.705 (0.141)	–
MD03	PS1-10blu	130.2135	45.2700	22.714 (0.208)	FAINT	MD08	PS1-10cei	240.1075	54.8165	–	INC
MD03	PS1-10cak	130.5093	43.9321	–	RED	MD08	PS1-11beu	240.7690	55.2721	23.440 (0.180)	INC
MD03	PS1-11gq	131.8921	43.7795	22.978 (0.250)	FAINT	MD08	PS1-10cej	241.7209	53.8874	23.530 (0.190)	VAR
MD03	PS1-11eh	131.4092	45.3290	23.177 (0.282)	FAINT	MD08	PS1-10cek	243.0319	55.1189	22.800 (0.150)	VAR
MD03	PS1-11qj	131.9785	45.2305	22.280 (0.166)	FAINT	MD08	PS1-11ben	244.4578	55.2028	23.960 (0.350)	FAINT
MD03	PS1-11hi	128.8228	44.5885	23.659 (0.269)	FAINT	MD08	PS1-10mn	241.1689	55.5560	22.673 (0.123)	INC
MD03	PS1-11rg	132.5940	43.9940	21.874 (0.100)	INC	MD08	PS1-10ne	244.1189	53.7972	21.097 (0.053)	VAR
MD03	PS1-11ol	130.8790	45.6951	22.822 (0.135)	FAINT	MD08	PS1-10aeo	242.0829	54.3316	22.732 (0.246)	FAINT
MD03	PS1-11ok	130.6385	45.7282	23.374 (0.257)	FAINT	MD08	PS1-10abn	240.3384	54.7644	22.739 (0.140)	FAINT
MD03	PS1-10ayc	132.3020	44.1192	23.315 (0.196)	INC	MD08	PS1-10aby	242.0255	53.7137	23.438 (0.189)	FAINT
MD03	PS1-10aww	130.3612	45.4012	22.829 (0.150)	INC	MD08	PS1-10abk	240.8492	54.0940	23.014 (0.236)	FAINT
MD03	PS1-11se	129.0951	43.6360	21.247 (0.053)	INC	MD08	PS1-11ug	241.9200	55.4232	22.538 (0.237)	FAINT
MD03	PS1-11sd	131.5120	43.4041	21.860 (0.151)	INC	MD08	PS1-11uc	240.5109	55.0289	22.700 (0.101)	FAINT
MD04	PS1-11ber	148.7119	2.5314	–	RED	MD08	PS1-11uf	244.1813	55.1709	22.571 (0.154)	FAINT
MD04	PS1-10tv	150.1942	1.3438	22.099 (0.258)	INC	MD08	PS1-10acg	245.0462	54.3438	–	RED
MD04	PS1-11cs	151.0165	1.0870	21.952 (0.095)	INC	MD09	PS1-10aak	333.4872	−0.7134	21.719 (0.129)	INC
MD04	PS1-11nv	150.4967	2.7301	22.541 (0.123)	FAINT	MD09	PS1-10aab	335.0863	0.5239	22.090 (0.129)	INC
MD04	PS1-11mv	150.6274	1.9906	22.076 (0.249)	FAINT	MD09	PS1-10bgx	333.8112	0.1249	23.490 (0.253)	FAINT
MD04	PS1-11mb	149.4433	0.8251	22.278 (0.166)	INC	MD09	PS1-10bma	333.1478	0.9874	22.657 (0.189)	FAINT
MD04	PS1-11vf	151.1440	2.1694	22.355 (0.139)	INC	MD09	PS1-10awi	333.9666	0.5064	22.731 (0.151)	FAINT
MD04	PS1-11tf	149.7141	0.6388	22.116 (0.131)	INC	MD09	PS1-10afy	333.7640	0.5902	23.187 (0.197)	FAINT
MD04	PS1-11bek	149.1747	2.7484	23.150 (0.180)	INC	MD09	PS1-11beo	334.6328	−0.0450	–	RED
MD04	PS1-11tl	149.6978	1.1330	22.519 (0.113)	INC	MD09	PS1-10cel	334.4344	−0.6454	23.070 (0.160)	FAINT
MD04	PS1-11tr	150.2001	1.3042	21.678 (0.083)	INC	MD09	PS1-11bep	332.7250	0.6546	22.920 (0.160)	FAINT
MD05	PS1-10ac	160.0895	57.9299	22.690 (0.154)	INC	MD10	PS1-10cem	352.6395	−0.0084	23.190 (0.140)	INC
MD05	PS1-11ck	160.2717	59.2027	22.379 (0.106)	FAINT	MD10	PS1-11beq	353.3164	0.0658	23.530 (0.350)	FAINT
MD05	PS1-10cec	164.2774	57.9606	23.120 (0.120)	INC	MD10	PS1-10cen	351.8198	−1.4149	22.760 (0.110)	FAINT
MD05	PS1-10ced	162.6750	57.4088	22.650 (0.170)	FAINT	MD10	PS1-10bja	351.3430	−0.7578	22.597 (0.127)	FAINT
MD05	PS1-10cee	163.5573	59.2589	22.800 (0.160)	INC	MD10	PS1-10bjy	351.1140	−1.1171	22.741 (0.192)	FAINT
MD05	PS1-11cb	162.0916	57.3682	22.525 (0.185)	FAINT	MD10	PS1-10bkg	352.9823	−0.8480	23.262 (0.200)	FAINT
MD05	PS1-11av	163.0888	57.3474	22.718 (0.256)	FAINT	MD10	PS1-10biw	350.9567	−0.0839	22.198 (0.141)	FAINT
MD05	PS1-11bm	162.6764	56.8736	22.541 (0.264)	FAINT	MD10	PS1-10aaz	351.3668	−0.3134	22.978 (0.248)	FAINT
MD05	PS1-11re	159.7510	58.7787	22.480 (0.139)	FAINT	MD10	PS1-10bnj	351.6292	−1.1867	23.330 (0.315)	FAINT
MD05	PS1-11ta	160.2264	58.4274	22.210 (0.144)	FAINT	MD10	PS1-10adf	353.3260	−0.7616	23.413 (0.264)	FAINT

This paper has been typeset from a TEX/LATEX file prepared by the author.